1 Fluid-mediated, brittle-ductile deformation at seismogenic depth:
2 Part I- Fluid record and deformation history of fault-veins in a
3 nuclear waste repository (Olkiluoto Island, Finland)

5 Barbara Marchesini[1§], Paolo Stefano Garofalo[1], Luca Menegon[2], Jussi Mattila[3] and Giulio Viola[1]
6
7 [1]Dipartimento di Scienze Biologiche, Geologiche e Ambientali, Università di Bologna, Italy
8 [2]School of Geography, Earth and Environmental Sciences, University of Plymouth, PL48AA Plymouth, UK
9 [3]Geological Survey of Finland (GTK), Espoo, Finland
10 *Correspondence to*: barbara.marchesini2@unibo.it

12 **Abstract.** The dynamic evolution of fault zones at the seismogenic brittle-ductile transition zone (BDTZ) expresses the delicate

13 interplay of numerous physical and chemical processes that occur at the time of strain localization. Deformation and flow of

14 aqueous fluids in these zones, in particular, are closely related and mutually dependent during cycles of repeating, transient

15 frictional and viscous deformation. Despite numerous studies documenting in detail seismogenic faults exhumed from the

16 BDTZ, uncertainties remain as to the role of fluids in facilitating deformation in this zone, particularly with regard to the

17 mechanics of broadly coeval brittle and ductile deformation. We combine here structural analysis, fluid inclusion data and

18 mineral chemistry data from synkinematic and authigenic minerals to reconstruct the temporal variations in P, T and bulk

19 composition of the fluids that mediated deformation and steered strain localization in a strike-slip fault from the BDTZ. This is

20 a fault formed within the Paleoproterozoic migmatitic basement of southwestern Finland, hosting in its core two laterally

21 continuous quartz veins formed by two texturally distinct quartz types – Qtz I and Qtz II, where Qtz I is demonstrably older

22 than Qtz II. Veins within the diffuse damage zone of the fault are infilled by Qtz I. Multi-scalar structural analysis indicates

23 recurrent cycles of mutually overprinting brittle and ductile deformation. Fluid inclusion microthermometry and mineral pair

24 geothermometry indicate that both quartz types precipitated from a fluid that was in a homogeneous state during the recurrent

25 cycles of faulting, and whose bulk salinity was in the 0-5 wt% NaCleq range. The temperature of the fluid phase involved with

26 the various episodes of initial strain localization and later reactivation changed with time, from c. 240 °C in the damage zone to

27 c. 350 °C in the core during Qtz I precipitation to < 200°C at the time of Qtz II crystallization. Fluid pressure estimates show an

28 oscillation in pore pressure comprised between 160 and 10 MPa during the fault activity stages. Our results suggest significant

29 variability in the overall physical conditions during the fault deformation history, possibly reflecting the interaction of several

30 batches of compositionally similar fluids ingressing the dilatant fault zone at different stages of its evolution, each with specific

31 T and P conditions. Initial, fluid-mediated embrittlement of the faulted rock volume generated a diffuse network of joint and/or

32 hybrid/shear fractures in the damage zone, whereas progressive strain localization led to more localized deformation within the

33   fault core. Localization was guided by cyclically increasing fluid pressure and transient embrittlement of a system that was

34   otherwise at overall ductile conditions.

35   Our analysis implies that fluid overpressure at the brittle-ductile transition can play a key role in the initial embrittlment of the

36   metamorphic basement and strain localization mechanisms.

38   **1 Introduction**

39   Physical and chemical properties of fault systems play a fundamental role in controlling the rheological behaviour of the Earth's

40   crust and in steering channelled fluid flow (e.g. Caine et al., 1996). Deformation and fluid flow are closely related and mutually

41   dependent via a number of feedbacks, such as the control that fluids exert upon the effectiveness of deformation processes and

42   the development of fault systems at all scales, and the control by rock heterogeneities and/or fracture system topology on the

43   net fault transmissivity (e.g. Crider and Peacock, 2004). The nucleation and development of permeable fault systems and the

44   mechanisms whereby individual faults may weaken and eventually fail are, therefore, complex functions of a number of

45   processes. In this perspective, the multiscalar interaction between fluid and mineral phases within fault rocks needs to be

46   studied with a system approach in order to single-out the roles and importance of all processes involved (Kaduri et al., 2017).

47   The most evident effect of fluid involvement, particularly in crustal volumes that have experienced large deformation-

48   controlled fluid fluxes, is the precipitation of authigenic and hydrothermal minerals within faults (Oliver and Bons, 2001 Viola

49   et al., 2016) and their immediately adjacent host rock (Mancktelow and Pennacchioni, 2005; Garofalo, 2004). In the

50   seismogenic region of the crust, where fluids may even be the primary driver of the seismic cycle (e.g Miller, 2013), faults have

51   been shown to have the potential to function like a "fluid-activated valve", whereby they experience transient and cyclic fluid

52   pressure build-up before sudden fluid venting, pore pressure- and mechanical strength drop concomitant with seismic failure

53   (e.g. Sibson, 1989, 1992b, 1993; Cox, 1995;Viola et al., 2006; De Paola et al., 2007; Wehrens et al., 2016). Hydrothermal ore

54   deposits, where fault networks focus relatively large volumes of ore fluids and precipitate economic minerals (Cox et al., 2001),

55   are also pertinent examples of significant deformation-controlled fluid ingress.

56   The seismogenic depth down to 10-15 km (e.g. Kohlstedt et al., 1995) is thus a key region of the crust where to study the whole

57   range of fluid-rock interaction processes occurring within fault zones. Deformation at that depth might be accommodated under

58   overall brittle-ductile conditions along fault systems crossing or rooting into the brittle ductile transition zone (BDTZ). In detail,

59   the deformation style in the BDTZ is generally characterized by the cyclicity, also at the short time scale, between brittle and

60   ductile behaviour. This is induced and regulated by the complex and transient interplay of numerous parameters, among which

61   the lithological composition and transient variation of temperature, pore pressure and strain rate within the deforming system.

62   Field studies have documented unequivocally that ductile and brittle deformation may even be simultaneously active during

63   deformation as a function of the transient and spatially heterogeneous evolution of the chemical and physical parameters

64   steering deformation, leading to the broad coexistence of geological features expressing frictional and viscous deformation

65   mechanisms and to mutual crosscutting relationships thereof (e.g., Guermani and Pennacchioni, 1998; Kjøll et al., 2015;

66   Pennacchioni et al., 2006 Wehrens et al., 2016).

67   Veins are particularly important in this context because they attest to the relative abundance of aqueous fluids in the

68   deformation history (e.g. Cox et al., 2001). Portions of the seismogenic crust that experience large fluid fluxes host large and

69   vertically extensive vein networks (Sibson et al., 1988), within which up to several millions of m^3 of hydrothermal minerals

70   may deposit from the flowing fluid (e.g. Heinrich et al., 2000; Cox, 2005; Bons, 2001; Garofalo et al., 2002). In contrast,

71   portions of the crust deforming in the absence of significant fluid flow would show scarce evidence of- or no veining, with only

72   synkinematic H_2O-rich minerals within the fault rock attesting to hydrous conditions (cf. Mancktelow and Pennacchioni, 2004;

73   Menegon et al., 2017).

74   The physical-chemical conditions of fluid-rock interaction in the BDTZ have been extensively studied within exhumed faults

75   by applying a set of geochemical tools that include fluid inclusion data (Ault and Selverstone, 2008; Garofalo et al., 2014;

76   Siebenaller et al., 2016; Compton et al., 2017), isotopic compositions of fault fluids and mass transfer calculations between host

77   rock and fault rocks (Goddard and Evans, 1995; Garofalo, 2004; Mittempergher et al., 2014; Spruzeniece and Piazolo, 2015).

78   These data yield important constraints on the PT conditions of fluid-rock interaction within the studied faults, on the source

79   region of the fluids reaching and flowing within the BDTZ and on element mobility during syn-tectonic fluid flow. These

80   studies, however, provide only limited information on the role of fluids on the potentially complex mechanisms that trigger and

81   permit the aforementioned cycles of brittle-ductile deformation. Open questions remain, such as, for example, which Pressure-

82   Temperature-Composition (PTX) conditions are best for a fluid to trigger brittle-ductile deformation cycles in a fault system

83   within the BDTZ, and which fluid property is specifically most effective in controlling the cycles.

84   In this work, we combine the meso- and microstructural observations with geochemical analysis of fluids, petrographic

85   documentation, microthermometric properties of fluid inclusion assemblages, electron probe microanalyses (EPMA) of fault

86   minerals, Raman spectrometry of fluid inclusions, and electron probe cathodoluminescence imaging to study the effects of

87   numerous cycles of fluid-rock interaction that have occurred in a vein-rich deformation zone from within the BDTZ of the

88   seismogenic region of the Paleoproterozoic continental crust of southwestern Finland. The studied deformation zone belongs to

89   an exhumed conjugate fault system that experienced a complex history of structural reactivation and fluid flow. Deformation

90   zone BFZ300, the target of our study, crops out at c. 426 m below sea level within the deep nuclear waste repository that is

91   presently being built in the island of Olkiluoto (Fig. 1a).

92   We show that this dataset constrains the physical and chemical conditions that prevailed at the time of fault initiation and

93   subsequent cyclic strain localization. The adopted integrated approach provides detailed and new insights into the mechanisms

94   steering deformation within the BDTZ. We propose a mechanical conceptual model that accounts for the constraints derived

95   from our multidisciplinary approach.

96   **2 Geological setting**

97   The study area is located in southwestern Finland, on the island of Olkiluoto (Fig.1a) within the Paleoproterozoic Svecofennian

98   orogenic province, which is characterized by supracrustal high-grade metamorphic sequences and plutonic rocks. The most

99   abundant lithologies in the study area are variably migmatitic metasedimentary rocks interleaved with metric levels of

100 metavolcanic rocks, calc-alkaline synorogenic TTG-type granitoids, and late orogenic leucogranites (Fig. 1a). For a detailed

101 lithological characterization of the area, we refer the reader to Hudson and Cosgrove (2007) and Aaltonen et al. (2016).

102 Numerous studies carried out on Olkiluoto have highlighted the long geological evolution of the region, which is commonly

103 summarised by tectonic models for the Paleoproterozoic evolution of southern Finland proposing either an evolution during a

104 single and semi-continuous Svecofennian orogenic event (Gorbatschev and Bogdanova, 1993) or, instead, a sequence of up to

105 five distinct accretion events leading to the amalgamation of several microcontinents and island arcs at the margin of the

106 Archean craton between 1.92 and 1.79 Ga (e.g. Lahtinen et al., 2005). In this scenario, several subduction systems developed,

107 and the collision of the involved microcontinents and island arc complexes resulted in conspicuous continental growth, forming

108 the major part of the Paleoproterozoic domain of the Fennoscandian Shield (1.89-1.87 Ga). According to Lahtinen et al. (2005),

109 this "Fennian accretionary event" ended with a phase of orogenic collapse associated with regional extension and remarkable

110 crustal thinning between c. 1.86 and 1.84 Ga. Renewed compression ensued during collision of the "Sarmatian Plate" with the

111 previously consolidated Svecofennian Shield, causing major crustal shortening, high temperature regional metamorphism

112 (Kukkonen and Lauri, 2009) and the emplacement of S-type granites (e.g. Ehlers et al., 1993). Tectonic activity ascribable to

113 this orogenic phase ceased with a new orogenic collapse at 1.79-1.77 Ga (Lahtinen et al., 2005).

114 Pervasive reworking of the Svecofennian domain took place in the Mesoproterozoic when the crust underwent significant

115 stretching and was intruded by voluminous Rapakivi granites and diabase dykes resulting from the widespread melting of the

116 lower crust at c. 1.65-1.50 Ga. This tectonic phase was probably due to the development of a rift along the present Baltic Sea

117 (Korja et al., 2001). Crustal thinning caused also the formation of the "Satakunta Graben", a NW-SE trending graben located c.

118 50 km to the north of Olkiluoto, which was later filled by Mesoproterozoic sandstone (Jotnian sandstones, Fig. 1a). The latest

119 stage of crustal evolution in southern Finland is expressed by the intrusion of 1.27-1.25 Ga, N-S striking olivine diabase dikes

120 (Fig. 1a; e.g., Suominen, 1991).

121 As to the structural evolution of the study area, the bedrock was affected by complex, polyphase ductile deformation between

122 1.86 and 1.81 Ga. According to the evolutionary deformation scheme proposed by Aaltonen et al. (2010) the results of up to

123 five different phases, referred to as D_1-D_5, are preserved in the local structural record, each characterised by structures with

124 distinctive mineral composition, metamorphic grade, geometry and kinematics. The most relevant phases to our study are D_2 to

125 D_4. During these ductile episodes, a regional and pervasive NE-SW striking and moderately SE-dipping foliation developed,

126 strain localized along mesoscopic shear zones parallel to subparallel to the foliation and extensive migmatization occurred

127 under amphibolite-facies metamorphic conditions. NNE-SSW and N-S striking mylonitic shear zones also formed under those

128 conditions, whereas later ductile events developed under progressively lower-grade metamorphism until c. 1.7 Ga ago, when

129 brittle deformation became the dominant deformation style in response to progressive regional exhumation and cooling (Mattila

130 and Viola, 2014; Aaltonen et al., 2016). The penetrative, inherited ductile grain that by then characterised the crystalline

131 basement and that was suitably oriented with regard to the prevailing stress field was invariably reactivated. This is the case for

132   several NNE-SSW striking faults mapped underground in the Onkalo repository, which clearly overprint earlier D4 shear zones

133   and fully exploit the pre-existing ductile precursors. Other faults, however, do not show any clear relation to the older ductile

134   fabric and cut it discordantly. The subvertical, dextral deformation zone we discuss in this paper, BFZ300, is a good example of

135   this.

136   In detail, BFZ300 belongs to a set of subvertical, conjugate brittle-ductile to fully brittle strike-slip faults characterized by N-S-

137   trending sinistral and NW-SE dextral faults. Both sets show a complex history of reactivation and contain evidence for cyclic

138   and transient switches between brittle and ductile deformation at all scales. Meso- and microstructural studies show that the

139   sinistral faults overprint and probably reactivate a dextral viscous precursor related to earlier, localized ductile deformation.

140   These faults locally contain pseudotachylyte injections, which attest to seismic behaviour during deformation (Menegon et al.,

141   2018). In contrast, dextral faults cut across the foliation, do not exploit any ductile precursors and do not host pseudotachylytes.

142   The fault zone studied here belongs to this second group of faults. In the following, we describe its architecture, reconstruct its

143   deformation history and constrain the deformation mechanisms and faulting conditions that acted during its nucleation and

144   subsequent development. The architecture and deformation history of the remarkably different conjugate structure of

145   BFZ300, which is a sinistral brittle ductile deformation zone, whose seismic brittle failure was steered by the presence of

146   a penetrative ductile precursor, will be described in a separate companion paper.

3 Applied methods

148   Field documentation and sampling were carried out at the underground BFZ300 exposures of Onkalo, which are necessarily

149   limited in extent but that, together with the logged diamond drill holes from the underground exploration, allow a well-

150   constrained 3D reconstruction of the local geology. The studied fault section is located at a depth of 426 m b.s.l. (Fig. 1b) and is

151   about 8 m long. To characterize the fault architecture and constrain the spatial and temporal association of fault rocks and the

152   type of fluid involved in the deformation, several outcrop samples, each representative of a distinct structural domain, were

153   collected at the outcrop (TPH-2, TPH-3, TPH-4, TPH-5and TPH-6), in addition to samples PH 21 and PH22 from a diamond

154   drill core that intersects BFZ300 at the same depth in an area that is currently not excavated (Fig. 3). From these samples we

155   prepared 10 petrographic thin sections (samples: TPH120-2, TPH 120-4, TPH 120-6, PH-21 and PH-22) and 9 doubly-polished

156   sections for fluid inclusion analysis (thickness: ~150 µm, samples: TPH120-2, TPH 120-4, TPH 120-6, PH-21 and PH-22). Due

157   to the extensive reactivation of the fault zone and the consequent obliteration of the FI record, FI study was carried out only in

158   samples TPH 120-4, TPH 120-6, PH-21. Hand samples and drill cores localities are specified in Fig. 2.

159   Microstructural work was carried out on oriented petrographic thin sections cut orthogonally to the foliation and parallel to the

160   striae that track the overall strike-slip kinematics of the deformation zone. Strie are defined by elongated trails of chlorite

161   grains, at the vein-host rock boundary.

3.1 Fluid inclusions and mineral chemistry

Fluid inclusion measurements were conducted on "fluid inclusion assemblages" – FIAs, i.e. on petrographically discriminated, cogenetic groups of fluid inclusions located along trails or (less commonly) within clusters (Bodnar, 2003a; Goldstein, 2003). By definition, FIAs are groups of inclusions that have been trapped together at a specific stage of mineral formation, and, as such, give the highest level of confidence when characterizing the properties of trapped fluids and discriminating possible stages of post-entrapment re-equilibration (Bodnar, 2003b, and ref. therein). We identified appropriate FIAs that constrain the deformation history of BFZ300, but also applied the Roedder's identification criteria of FIAs according to the timing of entrapment (i.e., primary, secondary, pseudosecondary) in order to link stages of fluid entrapment with stages of brittle and ductile deformation of quartz. In this regard, we can consider FI trails as synkinematic features, where FIAs are entrapped during stages of brittle deformation and fluid circulation, such that FIAs arranged along trails of the same orientation and with similar petrographic features might be representative of the same deformational event.

In the selected samples, we studied 12 FIAs entrapped within two distinct generations of quartz infilling two different generations of veins (named Qtz I and Qtz II, see description below) and exhibiting the least petrographic evidence of post-entrapment overprinting by later ductile and brittle deformation, which provided c. 400 microthermometric properties. Due to the well-documented tendency of fluid inclusions to modify their shape, volume, and composition after their initial entrapment even at low deviatoric stress conditions (e.g. Diamond et al., 2010; Kerrich, 1976; Tarantola et al., 2010; Wilkins and Barkas, 1978), working on FIAs that are as similar as possible to those preserving the pristine fluid conditions is essential when aiming at the study of the original physical and chemical properties of the fluid involved in the fault activity.

Microthermometric properties of fluid inclusions were determined at the Department of Biological, Geological and Environmental Sciences of the University of Bologna using a Linkam THMSG 600 heating/freezing stage coupled with an Olympus BX51 polarizing microscope. The microthermometry stage was calibrated by using synthetic fluid inclusion samples at –56.6, 0.0, and 374 °C, which correspond to the melting of CO_2, ice melting, and final homogenization of H_2O inclusions, respectively. Obtained accuracies were ±0.3 °C for final ice melting temperature (Tmice) and ±3 °C for final homogenization temperature (Thtot). In order to produce an internally consistent dataset, all phase transitions were exclusively collected for individual FIAs and measured by the same standard procedure. Samples were first rapidly cooled to c. -180 °C and then slowly heated to detect the potential formation of a solid carbonic phase, eutectic phases, salt hydrates, ice, and clathrates. The Thtot were later determined in the FIAs by heating the samples from room temperature and recording the mode of homogenization (i.e., by bubble or liquid disappearance). All phase transitions were measured by using the cycling method described by Goldstein and Reynolds, 1994, and care was taken in recording the minimum and maximum values for each assemblage. Volume fractions of individual fluid inclusions determined as % of the ratio $\varphi = Vv/Vtot$ (cf. Diamond, 2003), were estimated optically at room temperature using calibrated charts. Salinity, bulk densities and isochores were computed from the measured Tmice values using the HokieFlincs Excel spreadsheet (Steele-MacInnis et al., 2012 and reference therein).

194   Micro-Raman spectrometric analysis of fluid inclusions was carried out at the Department of Mathematical, Physical and

195   Computer Sciences of the University of Parma (Italy) using a Jobin-Yvon Horiba LabRam spectrometer equipped with He–Ne

196   laser (emission line 632.8 nm) and motorized XY stage. The spectral resolution of the measurements was determined as nearly

197   2 cm^{-1}. The confocal hole was adjusted to obtain a spatial (lateral and depth) resolution of 1–2 µm. Most spectra were obtained

198   with a 50× objective (N.A. 0.75), although for shallow inclusions also a 100× objective (N.A. 0.90) was used. The calibration

199   was made using the 520.7 cm^{-1} Raman line of silicon. A wide spectral range (100–3600 cm^{-1}) was scanned for each inclusion

200   for the presence of CO_2, N_2, CH_4, and H_2S, but the final acquisitions were made mainly between 1100 and 1800 cm^{-1} for the

201   study of CO_2 spectra, and between 2500 and 3300 cm^{-1} for CH_4 and H_2S. The acquisition time for each spectral window was

202   120–240 s, with two accumulations. The power on the sample surface is nearly 1 mW but the power on the analysed inclusions

203   has to be considered lower due to reflections and scattering. Analyses were carried out on the vapour bubbles of the fluid

204   inclusions.

205   After the calculation of representative fluid inclusion isochores for each FIA, the pressure corrections were assessed by using

206   the crystallization temperatures of two mineral pairs – namely chlorite-quartz and stannite-sphalerite – as independent input

207   parameters for Qtz I and Qtz II veins, respectively. Chlorite-quartz temperatures were calculated by using the method of

208   Bourdelle and Cathelineau (2015), which assumes quartz-chlorite equilibrium and uses ratios of chlorite end-member activities

209   to link the chlorite compositions with the corresponding formation temperatures through the quartz-chlorite equilibrium

210   constants. This method is based on the measurements of the concentrations of the major chlorite components (Si, Fe, Mg) and

211   can only be applied to chlorites with (K_2O + Na_2O + CaO) < 1wt%, indeed the case of our chlorites. To estimate the formation

212   temperature of cogenetic sulphides associated with Qtz II we used the stannite-sphalerite formation temperature following the

213   method proposed by Shimizu. and Shikazono (1985). This geothermometer uses the temperature dependency of iron and zinc

214   partitioning between stannite and sphalerite (Nekrasov et al., 1979) as a useful temperature indicator of the association Qtz II-

215   stannite and sphalerite.

216   **3.2 Electron Probe Microanalysis (EPMA)**

217   EPMA of fault minerals were carried out by using a JEOL-8200 wavelength-dispersive electron microprobe housed at the

218   Department of Earth Sciences of the University of Milan, Italy. The instrument fits 5 WDS spectrometers utilizing lithium

219   fluoride (LiFH), pentaerythritol (PETJ and PETH), and thallium acid pthalate (TAP) analysing crystals and an optical

220   microscope. Samples were probed with a beam size of ~1 µm at 15 keV and 5 nA beam current. Synthetic and natural materials

221   were used as calibration standards at the beginning of each session. Analytical 1-σ errors are typically < 4% for major elements

222   and for the minor elements.

223   Panchromatic cathodoluminescence (CL) imaging was performed by using the CL CCD detector adjacent to the optical

224   microscope of the JEOL-8200 on the sections used for microstructural work. The electron beam was focused on the sections

225   with an accelerating voltage of 15 kV and 30 nA beam current. Black/white digital images were collected with a 40x

226 magnification by beam mapping with the CCD detector at a spatial resolution of 1 μm (beam resolution), which resulted in

227 imaged areas of 27.8 x 22.2 mm. The exposure time for image acquisition was 120 s.

4 Results

4.1 BFZ300 fault architecture

230 BFZ300 strikes NNW-SSE and dips very steeply to subvertically to the southwest (Fig. 2a). It cuts through high-grade veined

231 migmatite, interlayered with gneiss and pegmatitic granite. At the studied underground outcrop with a length of 8 m, the fault is

232 a strike-slip fault system formed by two main subparallel fault segments connected by a mesoscopic step-over zone.

233 Subhorizontal striae and kinematic indicators such as chlorite slickensides and R and R' planes indicate invariably dextral

234 kinematics. The most striking mesoscopic characteristic of BFZ300 is the presence in the fault core of a composite set of almost

235 continuous quartz veins (between 1 and 20 cm in thickness) along the entire exposed strike length. A schematic representation

236 of the fault zone is shown in Figure 2.

237 The fault contains a 0.5-2 m thick damage zone separated by the host rock by two discrete bounding surfaces (Y planes

238 according to Tchalenko, 1970 Fig. 2a). The damage zone can be defined in the field on the basis of the presence of a fractured

239 volume containing sets of conjugate dextral and sinistral hybrid fractures (Fig. 2b) intersecting to form a tight acute angle of c.

240 38° (Fig.2a). Laterally continuous, NNW-SSE striking quartz-filled Mode I fractures (joints) invariably bisect this angle

241 (Fig.2ab), helping to constrain the stress field orientation at the time of fracture formation, with the greatest compressive stress

242 axis σ_1 parallel to the Mode I fracture strike and oriented c. NNW-SSE. Joints are sharp and have a regular spacing of c. 10 cm.

243 Quartz infilling the joints and the hybrid fractures of the damage zone forms veins up to 1-1.5 cm in thickness and is referred to

244 as Qtz I hereinafter. Its microstructural characteristics are described in detail below (Fig. 2b). Fractures and faults decorated by

245 Qtz I have a translucid look that reflect the generally fine grain size of Qtz I (< 1 cm, Fig. 3b.). Locally they are formed by en-

246 echelon tensional segments connected by shear planes not decorated by any quartz infill (Fig. 2c). Joints occur also as barren

247 fractures defining a penetrative sympathetic fracture cleavage (sensu Basson and Viola, 2004; stereonet of Fig. 2a). In general,

248 fracture density within the damage zone tends to increase towards the fault core.

249 The fault core is bounded by two main discrete slip surfaces (Y, Figs.2ae and 3a). It contains, and is defined by, two distinct

250 generations of quartz veins (Fig. 2d) that are interrupted and offset laterally by a metric step-over zone (Fig. 2e-g). The main

251 quartz vein of the core is infilled by quartz exhibiting the same microstructural characteristics of Qtz I in the damage zone; we

252 therefore refer to it as a Qtz I vein. It is accompanied by a younger, subparallel vein formed by a milky-white type of quartz

253 with a significantly larger quartz grain size than Qtz I (>1 cm) that we refer to as Qtz II (Figs. 2deg and 3). Locally, pockets of

254 cataclasite and breccia are also observed along and inbetween the two veins. Microstructural analysis reveals that they formed

255 at the expense of the host gneiss (Fig. 3bd). The Qtz II vein shows a quite irregular, curved geometry (Figs. 2d and 3c) and a

256 variable thickness up to a maximum of c. 20 cm. The minimum Qtz II vein thickness coincides spatially with a lateral apparent

257 displacement of the vein. The BFZ300 core varies in thickness between 20 and 30 cm along most of the exposed fault length,

258   but becomes thicker (up to 50 cm) in the compressional step-over zone that connects the two fault segments that are offset

259   laterally by c. 1 m. The step-over zone is defined by synthetic T fractures (Figs. 2eg) and contains a decimetric brecciated lens

260   (Fig. 2e). T fractures are generally filled by Qtz I veins (Fig. 2f).

261   Chlorite is present as a secondary phase, with a modal abundance between 5 and 10 vol% in both Qtz I and Qtz II veins. In Qtz

262   I veins it occurs as euhedral/subhedral crystals that are up to 1-2 mm in size. Chlorite is present mostly as a disseminated,

263   interstitial phase, concentrated mainly in the internal part of the vein. In the Qtz II vein, however, it occurs as elongated crystals

264   (5-8 mm in length) arranged perpendicularly to the walls of the vein, which suggests orthogonal dilation at the time of opening

265   (Fig. 3b). The Qtz II vein contains also small (1-2 cm) aggregates of sulphides (sphalerite, pyrite, galena, and chalcopyrite)

266   mainly concentrated in the central part of the vein (Fig. 3b). Qtz II-sulphide mineral associations and their textures are

267   described in detail below.

268   As observed in the field, the presence of Qtz I veins along the joints in the damage zone and the continuity of the fault core Qtz

269   I vein suggest Mode I fracturing during Qtz I emplacement (Fig.3ac). The semi-continuous parallelismQtz I and Qtz II veins in

270   the fault core, combined with the location of the Qtz II vein along the walls of the Qtz I vein, suggest the partial reactivation of

271   the Qtz I vein during Qtz II emplacement. Dilation leading to Qtz II emplacement exploited and further reworked the Qtz I-host

272   rock contact, that seemingly had lower tensile strength than the pristine migmatite. The reconstructed time relationship between

273   the two vein generations is also consistent with local evidence of the Qtz II vein partially crosscutting parts of the Qtz I vein

274   (Fig. 3a).

4.2 BFZ300 microstructural analysis

276   In the following we provide a description of the microstructural characteristics of BFZ300 by detailing our findings and

277   observations separately for the main structural domains of the fault zone.

278

279   4.2.1 Damage zone

280   Qtz I veins within the damage zone cut across the migmatitic host rock and form the infill of conjugate sets of hybrid fractures,

281   which, when studied at the microscale, appear as formed by dilatant segments joined by cataclastic shear fractures (Fig. 4a).

282   Shearing is well documented by the asymptotic bending into the shear surfaces of foliation planes formed by the alignment of

283   chlorite and muscovite, both partly altered to sericite and chlorite, respectively (Fig.4a). Qtz I infilling the tensional segments

284   has an average grain size between 200 µm and 3 mm and exhibits a rather heterogeneous texture, from purely blocky to mixed

285   elongated-blocky (Figs. 4bc). The largest crystals (800 µm to 1 mm) are elongated and stretch from the vein walls towards the

286   inner part of the vein (Figs. 4c and 5a), which is consistent with a syntaxial growth mechanism (Bons et al., 2012). At least two

287   episodes of vein growth/renewed dilation, as indicated by the presence of median lines (ML), are clearly visible within one of

288   the studied veins and confirm a syntaxial growth mechanism for the vein (Fig. 5). Medial lines are defined by the alignment of

289   chlorite, sericite, and carbonate aggregates (Fig. 5bc). Blocky euhedral quartz crystals are also found, with a grain size between

290   300 to 600 µm. These crystals are juxtaposed to very fine grained quartz (<200 µm) within sericite-rich cataclastic bands

291   (Fig.4b). These cataclasites contain also hydrothermally altered host-rock fragments including pervasively altered K-feldspar-

292   bearing lithic fragments and phyllosilicates.

293   With the exception of the blocky variety, Qtz I crystals exhibit various degrees of viscous deformation and recovery. They

294   contain widespread evidence of undulose extinction and extinction bands, indicating distributed internal plastic deformation.

295   Cathodoluminescence imaging of Qtz I shows the presence of a diffuse network of healed quartz microfractures (Fig. 4d),

296   which demonstrates healing subsequent to brittle deformation and fracturing.

297   Chlorite occurs as a disseminated phase within the Qtz I veins of the damage zone and in textural equilibrium with quartz. It has

298   a peculiar vermicular texture (Fig. 5b), crystal dimensions of about 100 µm, and displays interference colours ranging from

299   violet to Berlin blue. Vermicular chlorite forms small pockets mainly located in the central part of the veins and at the triple

300   junctions of blocky quartz crystals.

301   4.2.2 Fault core

302   In the BFZ300 fault core, the grain size of Qtz I is strongly variable within the vein, suggesting the presence of heterogeneous

303   and complex structural sub-domains of deformation. Qtz I has the smallest observed grain size (range: 30-800 µm, Fig. 6a) and

304   documents multiple and cyclic episodes of mutually overprinting brittle and ductile deformation leading to a complex

305   microstructural record. The earliest post-vein emplacement recognised deformation stage is reflected by the low-temperature,

306   intracrystalline deformation of the largest crystals (400-800 µm in size). Typical microstructures, such as undulose extinction,

307   wide extinction bands (WEBs, Derez et al., 2015), and bulging along grain boundaries are the most common microstructures

308   ascribable to this deformation stage (Fig. 6ab). A distinct, brittle deformation event is documented by narrow intracrystalline

309   fractures that crosscut the largest quartz crystals (Fig. 6bc), and which locally contain new grains of quartz ranging in size

310   between 20-100 µm (Fig. 6d). More in detail, these new grains form parallel bands that are oriented at low angle (<30°) to the

311   vein walls and that can be up to 2 mm in length and 200 µm in thickness. Plastically deformed Qtz I crystals hosting these

312   intracrystalline bands of new grains are cut across by a distinct set of subparallel intercrystalline fractures, which are interpreted

313   as the expression of yet another deformation event that occurred under overall brittle conditions. These fractures are parallel to

314   the strike of BFZ300 and are in turn healed by new quartz grains (grain size: 50-150 µm), and can be up to 2.5 cm in length and

315   up to 500 µm in width (Fig.6a). Their cathodoluminescence imaging shows that they are sealed and healed, yielding an

316   homogeneous dark cathodoluminescence signal.

317   Qtz II within the fault core is typically coarse grained (individual crystals: 300 µm-1 cm in size) and exhibits a regular blocky

318   texture devoid of any shape or crystal preferred orientation (Fig. 7a). Locally, these large crystals display primary growth

319   textures, such as primary FIAs oriented parallel to specific crystallographic planes. With the exception of undulose extinction,

320   Qtz II does not show clear evidence of plastic deformation, although cathodoluminescence imaging of optically continuous Qtz

321   II has also shown that a dense network of healed quartz microfractures locally crosscuts Qtz II crystals (Fig. 7c). These are

322   relatively thin (hundreds of µm thick) networks that are poorly visible to invisible by standard petrographic analysis. The only

323   petrographic evidence for these healed microfractures within quartz are well defined trails of fluid inclusions crosscutting

324   primary growth bands (Fig. 7d).

325   Chlorite is the second most abundant phase within the fault core Qtz I and Qtz II veins and occurs with a variety of textures.

326   Aggregates of vermicular chlorite similar to that occurring in the damage zone are also present in the Qtz I from the core (Fig.

327   8e), although chlorite with flaky and radiate textures (Fig. 8f) is also present. The latter type is generally 100-300 µm in size

328   and is in textural equilibrium with quartz and rare calcite. Radiate chlorite overgrowing fractured Qtz II (Fig. 7bc) suggests late

329   Qtz II precipitation. Associated with Qtz II, a sulphide assemblage made of pyrite, sphalerite, galena, and chalcopyrite (Fig.

330   7de, see also Fig. 3b) forms aggregates commonly located along quartz grain boundaries. In the studied sections, these

331   aggregates have dimensions between 10 and 600 µm. Chalcopyrite occurs as µm sized irregular inclusions within sphalerite

332   forming the typical "chalcopyrite disease" texture (e.g., Barton and Bethke, 1987; Fig. 7e).

333   Multiply reworked breccias and cataclasites crosscut BFZ300. In the studied sections, a cataclastic band between 5 and 8 mm

334   thick crosscuts both Qtz I and Qtz II veins (Fig. 8a), but is in turn crosscut by a different quartz-radiate chlorite vein displaying

335   evidence of syntaxial growth. This cataclasite contains poorly sorted and angular quartz clasts varying in size between 8 and 12

336   mm set in a finer (20-200 µm in size) white mica-quartz matrix. The largest quartz fragments show irregular, lobate grain

337   boundaries and are affected by undulose extinction. We interpret these textures as the product of dissolution and cataclastic

338   reworking of a previous generation, plastically deformed quartz.

339   Parallel sets of stylolitic seams strike N-S parallel to the strike of BFZ300 and mark the two sides of the cataclastic band (Fig.

340   9ac). They host anhedral sphalerite, stannite, galena, pyrite, and chalcopyrite (Fig. 9d), which are coeval with the formation of

341   Qtz II vein. We interpret the presence of these anhedral sulphide minerals along the stylolite as the product of passive

342   concentration by pression-solution processes. We use the stannite-sphalerite mineral pair as a geothermometer for Qtz II

343   emplacement.

4.3. Fluid inclusion data

345   The studied FIAs contain invariably a two-phase fluid (liquid-vapour) and are mainly arranged in secondary trails within Qtz I

346   crystals in the damage zone (Type S1) and also within Qtz I fault core, where they form dismembered (Type S2) trails and also

347   appear as individual clusters inside the crystals affected by viscous deformation (Type-S3). Within the Qtz II fault core, FIAs

348   are arranged as pseudosecondary (Type PS) and secondary (Type S4) trails. Representative examples of FI petrographic

349   features are shown for each BFZ300 structural domain in Fig. 9. Table 1 gives a schematic representation of the location of the

350   FI types presented above, in addition to their location in the fault architecture and their fluid properties.

351   *Damage Zone:* Within Qtz I grains (Fig. 9ab), secondary FIAs are found as trails (Fig. 9a) that parallel what we interpret as

352   healed, old intracrystalline microfractures. These microfractures are likely to be old joints and hybrid fractures whose

353   orientation mimics that of the mesosopic BFZ300 structural features. In these assemblages, FIs have a maximum size ranging

354   between 2 and 20 µm, a regular equidimensional shape (i.e. negative crystal morphology), and relatively uniform φ of 5-15%

355   (Fig. 9b).

356   *Fault Core:* Qtz I grains host secondary FIAs, which are transgranular trails (Fig. 9c) representing healed joints and hybrid

357   fractures. These trails are locally interrupted and dismembered by aggregates of new, fine-grained quartz grains (Fig. 9c), and

358   generate a texture that is indeed typical of Qtz I from the fault core (cf. Fig.6a). Fluid inclusions entrapped along these trails

359   (Type S2) vary in size between 1 and 10 µm, have a φ of 10-20%, and show a negative crystal morphology (Fig. 9d). Fluid

360   inclusions are also found as isolated clusters inside intensely recrystallised quartz domains (Fig. 9c). FIAs inside these

361   recrystallized quartz domains were pervasively obliterated during later episodes of ductile deformation. The development of

362   WEBs, intercrystalline bands and bulging (cf. Fig. 6) resulted in the transposition of these assemblages is invariably observed

363   and is documented, for instance, by the presence of short, secundary trails of regularly shaped inclusion oriented at a high angle

364   with respect to a longer, parent trail (Fig. 9c). Morphologically, these trails resemble the transposed trails documented in high-

365   grade metamorphic rocks (Andersen et al., 1990; van den Kerkhof et al., 2014). Different types of fluid inclusion morphologies

366   are found within the intensely recrystallized quartz domains (Fig. 9f). Negative crystal morphology is observed in some areas of

367   the selected samples, but it is uncommon. More typical is instead the "dismembered" morphology (cf: Vityk and Bodnar, 1995;

368   Tarantola et al., 2010), which is observed in the relatively large inclusions (> 20 µm). This morphology is made of a central

369   (often empty) inclusion, showing several tails and re-entrants, surrounded by a three-dimensional clusters of small "satellite"

370   inclusions. These clusters might be arranged with a quasi-planar geometry inside the host (i.e. in a trail-like fashion). Another

371   typical texture found in most assemblages is the "scalloped" morphology of small- to medium-sized inclusions (<10-15 µm),

372   which is defined by the presence of indentations, embayments, irregularities, and sharp tips of the inclusion walls (Fig. 9f).

373   Small inclusions (<1 µm) are also found at the edge of the straight, regular boundaries of new quartz grains; they are mostly

374   dark, i.e. they are vapour-rich or empty, and are equant in shape (Fig. 9e). Although small inclusions do not allow a

375   microtermometric study of the fluid-phase behaviour in this structural domain, they confirm the complex reactivation history of

376   BFZ300.

377   Qtz II contains both pseudosecondary (Type-PS) and secondary (Type-S4) assemblages (Fig. 9g-j). The first type is arranged in

378   trails, that cut at low angle the hosting quartz but not the neighbouring phases (e.g., chlorite, Fig. 9g). In these assemblages, FIs

379   are relatively large (2-45 µm). They show elongated shape and their φ varies between 15 and 30 % (Fig. 9h). Type-S4 FIAs

380   (Fig. 9i) have two-phase inclusions whose size (5-35 µm) is similar to that of PS trails, but show a φ between 30 and 40 %

381   (Fig. 9j).

382   Rare primary FIAs are also present along growth planes of Qtz II and are best observed predominantly in the least deformed

383   Qtz II crystals, where they have a relatively large size (20-50 µm). Elsewhere they present irregular and "dismembered"

384   textures, which suggest intense post-entrapment re-equilibration.

385 In summary, our microtextural study shows that the FIAs to be selected for the microthermometric study are only those hosted

386 within Qtz I and Qtz II crystals with the minimum degree of recrystallization and whose inclusions have textures corresponding

387 to the least intense post-entrapment re-equilibration (Bodnar, 2003b, and ref. therein; Tarantola et al., 2010). These are the

388 pseudosecondary and secondary FIAs in which dendritic or transposed inclusions are absent, and in which the host quartz

389 exhibits only undulose extinction (S1, S2, S4 and PS).

390 The majority of the secondary FIAs hosted within Qtz I from the damage zone show a range of Tmice between -5.9 and 0 °C,

391 which corresponds to a salinity of 0-9 wt% NaCleq (Fig. 10a). In these FIAs, final homogenization occurs by disappearance of

392 the vapour bubble and mainly between 150-330°C (Fig.10e). The secondary FIAs hosted within Qtz I of the fault core (Type-

393 S2) show a range of Tmice between -3.9 and 0 °C, which corresponds to salinities between 0 and 6 wt% NaCleq (Fig.10b), and

394 final homogenization by bubble disappearance is between 150 and 420°C (Fig.10f).

395 The Type PS FIAs show a range of Tmice between -11 and 0 °C, which corresponds to a salinity range of 0-15.2 wt% NaCleq

396 (Fig.10c), and Thtot by bubble disappearance is comprised between 150 and 440°C (Fig.10g). The Type S4 FIAs have a range

397 of Tmice between -7.3 and 0 °C, which corresponds to a 0-10.9 wt% NaCleq range of salinity (Fig.10d), while final

398 homogenization by bubble disappearance is comprised between 150 and 430°C (Fig.10h). Final homogenization occurs always

399 by bubble disappearance.

400 Raman spectra from the vapour phase of fluid inclusions hosted by the Qtz I and II show peaks at the characteristic

401 wavenumbers of CH_4 (2917 cm^{-1}), and CO_2 (1388 cm^{-1}). These peaks were determined as weak in all spectra, and CO_2 detection

402 was only sporadic in one of the sample of the fault core (TPH-120 4A). Such spectroscopic determinations are consistent with

403 the lack of microthermometric evidence for CO_2 or CH_4 occurrence in the FIAs, i.e., with the failure to detect melting of a

404 carbonic phase or clathrate hydrates during the freezing experiments (cf. Rosso and Bodnar, 1995; Dubessy et al., 2001). The

405 impossibility to detect CO_2- and CH_4-bearing fluids via microthermometric determinations indicates a gas pressure in the

406 analysed inclusions that is systematically lower than that required to observe clathrate dissociation (e.g., 1.4 MPa in CO_2-H_2O

407 fluids, Rosso and Bodnar, 1995), i.e. it shows low gas concentrations. Considering the broad salinity range of 0.1-14 wt%

408 $NaCl_{eq}$ for the BFZ300 fluids (which corresponds to NaCl concentrations of 1.7 10^{-3} – 2.4 M), we cannot estimate a maximum

409 CH_4 concentration.

410 **4.4 Chlorite and sulphide geothermometry**

411 Chlorite composition has been determined for several generations of chlorites in association with Qtz I and II, namely

412 vermicular chlorite associated with Qtz I from the damage zone, vermicular and radiate chlorite associated with Qtz I from the

413 fault core, and radiate chlorite associated with Qtz II from the fault core (Table 2). The EPMA data show that, in general, the

414 BFZ300 chlorites are Fe-rich (XFe = Fe/(Fe+Mg) between c. 0.65 and 0.90), have concentrations of (Na_2O+K_2O+CaO) <1

415 wt%, and result mainly from a solid solution of the sudoite and daphnite end-members, i.e., of $Mg_2Al_3(Si_3Al)O_{10})(OH)_8$ -

416 $(Fe,Mg)_5Al(Si,Al)_4O_{10}(OH)_8$. The dataset shows in particular that the compositions of the distinct chlorite generations vary

417 systematically with vein generation, as shown by the vermicular chlorite associated with Qtz I veins (Fig. 8e) with a XFe

418 between 0.65 and 0.67 and the radiate chlorite associated with Qtz I from the fault core and Qtz II (Figs. 8f and 7b) with a XFe

419 between 0.76 and 0.86.

420 Temperature-composition relationships for the quartz-chlorite pair portrayed in the T-R^{2+}–Si diagram of Bourdelle and

421 Cathelineau (2015) show that, in the hypothesis of quartz-chlorite equilibrium, the precipitation of vermicular chlorite within

422 the Qtz I of the damage zone took place in the 175-250 °C range (green diamonds of Fig. 11a). This range is distinct from that

423 of the vermicular and radiate chlorite from Qtz I of the fault core, which is probably >350 °C because the measured R^{2+}–Si

424 compositional parameters (R^{2+} = Mg+Fe) plot at the edge of, or slightly outside, the calibrated region of the Bourdelle and

425 Cathelineau plot (red diamonds of Fig. 11a). We stress that the high-T chlorite plots parallel to the 350 °C isotherm, suggesting

426 that it precipitated most probably at the same, or at a similar, temperature. Radiate chlorite associated with Qtz II from the fault

427 core is instead compatible with an equilibrium precipitation at 160-200 °C (light-blue diamonds in Fig.11a).

428 The collected EPMA data show that the sulphides associated with Qtz II have compositions that approach those of pure phases

429 (Table 3). Pyrite has trace element concentrations (Cu, As, Pb, Ni, Zn) that are in general below the EPMA detection limit,

430 while galena, sphalerite, and chalcopyrite show only some significant trace contents of Fe and Zn (e.g., Fe: 0.22-1.00 wt% in

431 galena; Zn: 0.11-3.95 wt% in chalcopyrite). Pyrite and sphalerite from the Qtz II veins (Fig. 7e) have trace element

432 concentrations that are, again, mostly below detection limits.

433 The stylolites bordering the cataclasite bands described above and formed at the contact between the Qtz I and Qtz II vein

434 contain pyrite, galena, and the sphalerite-stannite pair (Fig. 8acd), with the latter showing the largest compositional variation.

435 This pair represents a mineral geothermometer because the partitioning of Zn and Fe between sphalerite and stannite was

436 demonstrated to be temperature dependent but pressure independent (Nekrasov et al., 1979; Shimizu, M. and Shikazono, 1985).

437 In the fourteen analysed pairs, stannite shows a range of Zn concentrations varying between 0.48 wt% and 3.25 wt%, while

438 those of Fe, Cu and Sn vary within narrow ranges (Fe: 12.74±0.56 wt%; Cu: 28.30 ±0.33 wt%; Sn: 27.65 ±0.71 wt%).

439 Sphalerite in the pair has concentrations of Fe and Zn of 7.63±0.87 wt% and 56.68 ±1.17 wt%, respectively. These ranges allow

440 the calculation of the partition coefficient (K_D) of the reaction: Cu_2FeSnS_4 (in stannite) + ZnS (in sphalerite) = Cu_2ZnSnS_4 (in

441 stannite) + FeS (in sphalerite). We have used the logK_D–T relationship of Shimizu and Shikazono (1985) to calculate the

442 formation temperature of the pair, which is portrayed in the ($X_{Cu2FeSnS4}/X_{Cu2ZnSnS4}$)-($X_{FeS}/X_{ZnS}$) plot of Shimizu and Shikazono

443 (Fig. 11b). The resulting 220-305 °C interval lies at the low end of, or slightly outside, the 250-350 °C interval of the

444 geothermometer. Therefore, while the 250-305 °C interval can be taken as an estimation of the formation T of sphalerite-

445 stannite in the stylolite, the 220-250 °C interval should be taken with caution.

446 **5 Discussion**

447 Our work constrains the structural architecture and the environmental conditions at which BFZ300 deformation took place.

448 Field and petrographic observations support the idea of transiently elevated fluid pressures, cyclic frictional-viscous

449 deformation and progressive, yet discrete strain localization (Figs. 2 and 3). Analytical data suggest that these deformation

450 cycles took place at the BDTZ. In the following, we discuss these constraints by systematically considering our different

451 analytical results.

5.1. Fluid inclusion data and mineral-pair geothermometry

453 Microthermometric and Raman spectrometry data show that the fluid entrapped within the studied FIAs at the time of formation

454 of the damage zone and fault core during precipitation of Qtz I and Qtz II veins can be represented by a H_2O-NaCl model fluid.

455 The fluid was in a homogeneous state at the time of entrapment, as testified by the consistent final homogenization by bubble

456 disappearance. It also had a low bulk salinity, as shown by the distribution of >80% of the ice melting (Tmice) measurements

457 skewed towards values of –3 °C or higher, which corresponds to bulk salinities of 5 wt% $NaCl_{eq}$ or less (Fig. 10a-d).

458 The documented Thtot varies between c. 150 and 430 °C without a single mode or a skew (Fig. 11e-h). Such distribution shows

459 that no common range of entrapment temperatures can be identified in the entire dataset, and that the properties of individual,

460 well-identified FIAs do not correspond to those of well-preserved assemblages. Indeed, the ranges of Thtot in individual FIAs

461 are typically of the order of 150-200 °C (Fig. 10e-h), i.e. a value that is much higher than the ~10 °C range expected for

462 homogeneous FIAs entrapped isochorically and isoplethically (Fall et al., 2009; Vityk and Bodnar, 1998) and that demonstrates

463 post-entrapment re-equilibration (cf. Bodnar, 2003b; Sterner and Bodnar, 1989).

464 A major implication of fluid inclusion re-equilibration in our study is that the calculated fluid properties do not rigorously

465 reflect those of the pristine fluid originally entrapped within BFZ300, but rather that of a fluid that modified its properties

466 during the fault activity. This is comparable to the results of other fluid inclusions studies from faults (Boullier, 1999; Garofalo

467 et al., 2014; Roedder, 1984).

468 In spite of these difficulties, a possible approach to interpret our FI dataset is the comparison with the experimental work on

469 synthetic fluid inclusions subjected to a range of post-entrapment re-equilibration conditions (Bakker, 2017; Bakker and Jansen,

470 1990, 1991, 1994; Vityk and Bodnar, 1995, 1998; Vityk et al., 1994). Such comparison is in our case difficult because most

471 experimental work was carried out at high TP conditions (500-900 °C; 90-300 MPa) and also because only few experiments

472 were carried out under deviatoric stress conditions that approach those of natural rocks (Diamond et al., 2010; Tarantola et al.,

473 2010). Despite these limitations, however, some key experimental results provide fundamental constraints on our dataset. First,

474 both hydrostatic and uniaxial compression experiments showed that in each re-equilibrated FIA a number of inclusions survive

475 virtually intact the modified post-entrapment PT conditions, showing that only severe deformation brings to total re-

476 equilibration and complete obliteration of pristine inclusions (i.e., Δσ>100 MPa in uniaxial compression experiments; >400

477 MPa change of confining P in hydrostatic experiments). Second, under conditions leading to only low to moderate re-

478 equilibration, the bulk chemical composition of the fluid inclusions does not change significantly from that of the pristine

479 inclusions.

480   All of this implies that natural quartz samples with microstructures typical of moderate T deformation, such as deformation

481   lamellae, deformation bands, undulose extinction and bulging, and hosting FIAs with moderately re-equilibrated textures,

482   should still contain a number of inclusions whose properties resemble those of the pristine fluid. Thus, it is possible that an

483   aliquot of the 1-5 wt% NaCleq FIAs from Qtz I and II crystals from both the damage zone and fault core is still representative

484   of the pristine sampled fluid. These inclusions would be those that survived or were relatively less affected by deformation

485   events postdating their entrapment. Inclusions falling outside the most typical 1-5 wt% NaCleq salinity range would instead

486   correspond to those that experienced significant H_2O loss and consequent salinity increase during the successive stages of fault

487   deformation (cf. Bakker and Jansen, 1990; Diamond et al., 2010). The large documented range of Thtot lacking a specific mode

488   observed in individual FIAs is the product of fluid density changes caused by fluid inclusion re-equilibration during post-

489   entrapment deformation. This would have happened repeatedly and cyclically within the host quartz during all ductile and

490   brittle stages of deformation of the multi-stage deformation history of BFZ300. The cumulative effect of these cyclic events on

491   fluid inclusions causes the impossibility to determine the exact T_f and P_f at entrapment; however, the ranges of PT values that

492   approach the true PT conditions can be assessed with some degree of confidence. Therefore, we suggest that the 200-350 °C

493   Thtot interval (Fig. 10 e-h) of the 1-5 wt% NaCleq fluid might reflect the characteristic range of the vast majority of damage

494   zone and fault core fluid. This value overlaps with the 175-350 °C range estimated with the quartz-chlorite geothermometer

495   (Fig. 11a) and the 220-305 °C range estimated with the sphalerite-stannite geothermometer (Fig. 11b).

496   Fully aware of these limitations, we have combined the microthermometric data of the studied FIAs with the independent

497   quartz-chlorite and sphalerite-stannite geothermometers to constrain the most probable P_f during faulting events. With this

498   approach, we use the formation temperatures of the mineral pairs as independent geothermometers and consider the intersection

499   between these values and the FIA isochores to derive the ranges of trapping pressure (cf. Roedder and Bodnar, 1980). In Fig.

500   12, we present the P_f ranges that are calculated using the entire salinity range of the studied FIAs (cf. Fig. 10); however, we

501   highlight the most probable P_f ranges that are consistent with what we consider best preserved salinity range (0-5 wt% NaCleq).

502   Accordingly, for the damage zone we estimate a P_f interval of 20-90 MPa (Fig.12a) by intersecting the range of T obtained

503   from the chlorite-quartz pair in the damage zone Qtz I (T c.170-240 °C, Fig. 11a) with the range of isochores from the same

504   quartz. As to fluid pressure estimations in the fault core, we combine the 350 °C obtained from the chlorite-quartz pair from the

505   fault core Qtz I (T>350 °C are outside the calibrated range of the geothermometer) with the ranges of isochores from the same

506   quartz, from which we obtain P_f ranging between c. 140 and 120 MPa (Fig. 12b). Similarly, the intersection between the

507   equilibrium T of the sphalerite-stannite pair in the Qtz II fault core (250-305 °C) and the range of isochores of the Type PS

508   FIAs of Qtz II (Fig.9) defines P_f values ranging between 10 and 140 MPa (Fig.12c). Estimations from Type-S4 FIAs (Fig.9)

509   constrain a range between 40 and 160MPa (Fig. 12d). We propose that these values are sufficiently accurate to constrain

510   multiple stages of fault slip, each one triggered by a fluid pulse having a distinct pressure. Hence, fault activity started at 200 °C

511   and at P_f varying between 20 and 90 MPa and continued through higher temperatures (305-350 °C) and P_f (120-160 MPa).

5.2. Structural evolution and fluid flow

Based on the integration of field, microstructural, thermometric and fluid inclusions constraints (Table 1), we propose a conceptual model for the structural evolution of BFZ300 (Fig. 13). The fault's finite strain results from several slip episodes mediated by multiple events of fluid ingress and fluid-rock interaction. A first constraint provided by our study is that the bulk chemical composition of the fluids that flowed within the fault did not change significantly during the documented fault activity, as the best preserved 0-5 wt% NaCleq salinity range points to a compositionally homogeneous fluid. This suggests a compositionally homogeneous source region of the fluid, or, alternatively, that the studied section of the fault did not interact with fluids of substantially different composition.

The embrittlement of the Olkiluoto metamorphic basement (time t_1 of Fig. 13ab) represents the initial stage of the deformational history of BFZ300 when conditions for brittle dilation and fracturing of the Paleoproterozoic basement were first met in a transien fashion. We propose that brittle failure under still ductile environmental conditions was caused by transiently elevated P_f, as demonstrated by field evidence of hydrofracturing (Figs. 2 and 3) and the pore pressure estimations (Fig. 12 and Table 1). Hydrofracturing of the host basement is also expressed by the emplacement of Qtz I veins along the diffuse network of joints and conjugate hybrid/shear fractures of the damage zone (Figs. 13a and 2g). These brittle features are quite evenly distributed within the damage zone suggesting initial volumetrically diffuse strain distribution. Their formation caused the overall mechanical weakening of the actively fracturing host rock volume, which in turn facilitated later strain localization. Brittle structures formed during this stage are discordant to the ENE-WSW striking metamorphic foliation (Fig. 1b), which they cut at high angle (Fig. 13a). Conditions for tensional and hybrid failure require low differential stress, i.e. $\sigma_1 - \sigma_3 \sim 4T$, where T is the tensional strength of the rock. Opening of fractures caused a stress drop, sudden increase of permeability, fluid venting and inhibited further build-up of P_f. Dilatant fractures were partially infilled by Qtz I, precipitated from a first pulse of the low-salinity fluid. Crystallization of Qtz I and formation of veins within these fractures caused hardening of the system. The progressive recovery of shear stresses concomitant with the progressive sealing of dilatant fractures altered the overall background stress conditions such that failure, after causing initial pure dilation, was accommodated by hybrid extensional failure and, eventually, by shear fracturing (Fig. 13b), thus forming laterally continuous and interconnected shear fractures associated to breccia pockets and cataclasites (Figs. 2e and 3bd). Conjugate shear fractures connected the previously formed extensional fractures through a fracture coalescence mechanism (e.g. Griffith, 1921; Fig. 13a). At the micro-scale this is demonstrated by the elongated blocky texture of Qtz I crystals from the damage zone (Fig. 11), where crystals grew at high angle to the vein boundaries (thus suggesting initial near-orthogonal dilation) and are physically connected by cataclastic shear bands to form a fault-fracture mesh (e.g.Sibson, 1996; Figures 4ab). Cataclastic bands formed at the expense of the migmatitic host rock are enriched in authigenic, synkinematic sericite, likely due to the interaction between K-feldspar and fluids circulating in the dilatant fault zone (Fig. 4b). Shear fractures thus deformed the migmatitic host rock to connect dilatant and mostly Qtz I-filled tension gashes during a continuum of deformation. The conjugate shear fractures ascribable to this stage

544   invariably define tight acute angles (Fig. 2b), which we take as further evidence of overall low differential stress conditions at

545   the time of failure (Fig. 13b).

546   In synthesis, Qtz I veins from the damage zone are interpreted as the expression of the earliest stage of fault nucleation, before

547   strain localization affected a progressively narrower rock volume to eventually form the main fault core. Indeed, Qtz I in the

548   damage zone preserves mostly brittle microstructures and lacks a pervasive ductile overprint, which is instead prevalent within

549   the fault core. As a consequence, we interpret the chemical properties of the fluid derived from these veins as the closest to the

550   initial conditions of the first fluid involved in BFZ300 nucleation. Fluid inclusion and geothermometric estimations from the

551   sinkinematic chlorite crystals associated with the damage zone Qtz I (Figs.5a and 11a), suggest chlorite precipitation at a T of c.

552   200° C and P_f between c. 90 and 20 MPa at the time of fault nucleation. Based on geometric, kinematic and deformation style

553   characteristics, we assign this deformation episode to Stage 1 by Mattila and Viola (2014) (their Fig. 18), i.e. to a discrete brittle

554   episode that they consider the expression of the earliest onset of brittle conditions in southwestern Finland c. 1.75 Ga ago, under

555   overall NW-SE to NNW-SSE transpressive conditions.

556   Further deformation of the BFZ300 (time t_2 of Fig. 13c) occurred by progressive inward strain localization and narrowing of the

557   actively deforming volume of the deformation zone (from a wide damage zone to a narrow fault core). The early BFZ300 core,

558   consisting of the main Qtz I vein is interpreted as having formed at this stage, within an overall dextral strike-slip kinematic

559   framework. Emplacement of the Qtz I vein in the core represents the last pulse of this brittle deformational episode (Fig. 13b).

560   Major fluid venting was likely associated with it, such that the system, once brittle failure in the core had occurred by

561   hydrofracturing, moved back to a more diffuse deformation style typical of the still prevailing ductile conditions. Microscopic

562   evidence of ductile deformation by dynamic recrystallization (Fig. 6ab, Table 1) overprinting the early brittle structures of Qtz I

563   in the fault core supports slow strain rate conditions during deformation. However, this viscous background deformation was

564   punctuated by renewed and cyclically transient embrittlement as documented by healed fractures shown by trails of secondary

565   fluid inclusions cutting across both the ductile fabrics and the earlier brittle deformational features (Fig.6c, d and e). Repeated

566   pulses of high P_f (120-140 MPa) likely triggered these brittle-ductile oscillations. Repeated fluid ingresses and related

567   deformation would, in addition, also have caused some of the post-entrapment equilibration of the FI, as discussed above.

568   The cycles of brittle and viscous deformation may be explained as follows. Cyclic brittle failure would have repeatedly lowered

569   P_f, which lowered the background stress and strain rate and favoured ductile deformation by dynamic recrystallization at T >

570   300 °C between the slip events (e.g. Passchier and Trow, 2005). The fault regained cohesive strength after each brittle failure

571   episode through vein formation and sealing/healing of the fracture networks. Porosity destruction by mineral crystallization and

572   fracture sealing, as clearly shown by CL imaging (Fig 4d), induced a progressive reduction of permeability and mechanical

573   healing of the fault, which promoted an increase of P_f and ultimately triggered a new brittle failure. Therefore, pore pressure

574   build-up promoted episodic brittle fracturing followed by cementation and plastic deformation/recovery. The compelling

575   evidence for this deformation occurring at T ≈ 350° C indicate that the described processes identify the BDT of the quartz-

576   feldspathic crust (Kohlstedt et al., 1995).

577   Mattila and Viola (2014) described a second brittle stage (referred to as Stage 2, their Fig. 18) during which a c. N-S to NNE-
578   SSW-oriented episode of transpressional deformation affected southwestern Finland. Geometric and temporal relationships
579   between structures of Stages 1 and 2 (see also Viola et al., 2009) were used to infer a clockwise rotation of the horizontal
580   compression direction from NW-SE (Stage 1) to NNE-SSW (Stage 2). Consistent with the kinematic framework of Stage 2, we
581   propose here that during progressive regional exhumation and cooling to entirely brittle conditions, the BFZ300 deformation
582   continued through a further, distinct deformation phase (t_3 of Fig. 13e). This stage accommodated the selective reactivation of
583   the BFZ300 core, with renewed dilation due to the rotated σ_1 during Stage 2 acting subparallel to the strike of the Qtz I vein in
584   the BFZ300 core. Localised dilation in a still fluid-rich system allowed the emplacement of the Qtz II vein (Fig. 13e). Our
585   estimations indicate that P_f and T conditions at that time were between 140 and 10 MPa and T $\approx$ 305° C, respectively. The
586   BFZ300 core was reactivated under overall hybrid conditions (Fig. 13f), as suggested by the irregular thickness and curved
587   geometry of the Qtz II vein therein, and by the synkinematic chlorite crystals that are stretched orthogonally to the vein
588   boundaries (Fig. 3c). The Qtz II vein invariably localized along at the contact between Qtz I and the host rock (Figs. 2, 3 and
589   13e) suggesting selective reactivation along the pre-existing principal slip zones (Riedel shears and boundary shears,
590   Tchalenko, 1970), which represented the weakest part of the fault (strength profile Fig. 13h). Evidence for mesoscale hybrid
591   fracturing and our P_f estimates (Fig. 11) suggest that P_f was lower than that of the earlier deformation stages.

592   BFZ300 underwent one or more events of brittle fracturing and induration (Fig.13g), as suggested by CL imaging of Qtz II
593   crystals (Fig.7c). Fluid pressure estimations for this structural phase are between 160 and 40 MPa.

594   The stylolitic seams having a strike parallel to the BFZ300 fault zone suggest a direction of maximum compression (σ_1)
595   oriented c. E-W, i.e. subparallel to the inferred Sveconorwegian main shortening direction (e.g., Viola et al., 2011). The
596   sphalerite-stannite mineral pairs arranged along these structures are supposed to be concentrated through a pression-solution
597   mechanism during this deformational stage.

598   Skyttä and Torvela (2018) proposed that BFZ300 is a brittle structure localized onto a zone of incomplete structural
599   transposition inherited from the earlier ductile history of the Olkiluoto basement. However, in our mesoscale and
600   microstructural analysis we did not find evidence of any ductile precursor, and we note that BFZ300 cuts the ductile structural
601   grain at high angle, which excludes any reactivation of precursor ductile fabrics.

602   **5.3. Implications for seismic deformation at the base of the BDTZ**

603   This study demonstrates the role of overpressured fluids on strain localisation during the incipient stages of fault nucleation and
604   subsequent reactivation(s) at the BDTZ. The maximum estimated PT conditions derived in this study (peak conditions of 160
605   MPa and 350 °C) are indeed realistic for the base of the seismogenic zone in the continental lithosphere (e.g., Scholz, 1990, and
606   references therein) where the brittle-ductile transition for quartz occurs.

607   Mechanical models of long-term deformation (Rolandone and Jaupart, 2002) propose that deformation at the brittle-ductile
608   transition can be reasonably described as being mostly accommodated by intermittent and concomitant coseismic slip and

609   ductile flow. Major hydrofracturing, as that documented in this study by the Qtz I and II veins, is possibly related to seismic

610   failure. Faults accommodating hydrofracturing are indeed commonly interpreted as seismogenic (e.g.Sibson, 1992a; Cox, 1995)

611   particularly at depth, where the reactivation of misoriented faults is only possible for fluid pressures exceeding σ_3 (e.g. Sibson,

612   1985).

613   Our study confirms this view because BFZ300 contains not only brittle fault rocks overprinting and overprinted by veins, but

614   also clearcut evidence of mutually overprinting brittle and ductile deformation (Fig.6). In the light of the field observations

615   discussed and of the constraints derived, we suggest therefore that BFZ300 behaved in a seismic way at least during the

616   emplacement of the principal Qtz I and Qtz II veins. Hydrofracture veins are largely interpreted in the literature as the evidence

617   of earthquake in fluid-rich faults (Cox, 1995).

618   In this perspective, two possible scenarios can be considered to explain the genetic relationships between BFZ300 and a

619   possible seismic behaviour of the crust during the Svecofennian orogeny. In a first scenario, the quartz veins of the fault core

620   would represent the result of coseismic rupture during the mainshocks of a fully developed seismic cycle. Pore pressure

621   fluctuations caused the repeated transient embrittlement of the rock mass, wich was otherwise under overall ductile conditions.

622   The documented brittle-ductile cycles are thus the expression of coseismic fracturing and aseismic creep between the individual

623   shocks, as shown by viscous deformation overprinting the brittle features, guided by the residual differential stress.

624   A second possibility is that faulting occurred in the absence of a well-defined sequence of main- and aftershocks. As in the case

625   of man-induced earthquakes triggered by high-pressure fluids during injection of fluids (e.g. Healy et al., 1968), where

626   deformation is typically accommodated by diffuse swarms of low magnitude seismicity rather than well-defined mainshock-

627   aftershock sequences (Cox, 2016), we propose that BFZ300 might have localised strain by diffuse veining with crack and seal

628   textures (Cox, 2016). Breccias and cataclasites (Fig.s 3 and 8) mutually overprinting with veins show that failure and veining

629   were indeed broadly coeval (e.g. Cox, 1995; Cox, 2016). Healing in fluid-rich environments can occur over short periods of

630   time (days-months) when compared with recurrence time of large earthquakes (10-100 years) (Olsen et al., 1998; Tenthorey

631   and Cox, 2006). Therefore, the documented repeated switches between brittle and ductile deformations would then be steered

632   again by transient episodes of fluid overpressuring but in this case would express the accommodation of swarms of minor

633   background earthquakes within overall ductile conditions.

634   Microstructures of fault-rocks exhumed from the brittle-ductile transition in other geological settings, are mostly in agreement

635   with our hypotheses of seismic deformation. Transient and short term high-stress deformation followed by phases of stress

636   relaxation, which is prevalently characterized by recovery and recrystallization processes, has been documented by several

637   authors in deformed quartz (Trepmann and Stöckhert, 2003; Trepmann et al., 2007; Bestmann et al., 2012; Trepmann and

638   Stöckhert, 2013; Trepmann et al., 2017).

639   To conclude, BFZ300 represents an interesting case of likely seismic deformation within a fluid rich system at the base of the

640   seismogenic crust. The absence of later, thoroughgoing and high-strain, potentially obliterating deformation episodes allows the

641   documentation of a complex structural evolution, from the earliest localisation to the mature structural stage.

6 Conclusions

Our analysis shows that a multi-disciplinary, multi-technique study of faulting initiation and evolution has indeed the potential to provide useful insights into the complex and cyclic processes of fluid-fault interaction and effects thereof at the base of the seismogenic crust. It further constrains, moreover, the importance of cyclic seismicity and fluids in the fragmentation of Precambrian cratons when deformed at the brittle-ductile transition zone, something that is not yet that well understood for the Fennoscandian Shield. Our study, moreover, provides potentially important inputs to many modern geological applications, including site characterization of deep geological disposal facilities for spent nuclear fuel. Results from the detailed geological characterization of faults at the Olkiluoto site can thus be used toward the continuous updating of the geological site description and yield further constraints on the mechanics of faulting at those conditions and at that time.

References

Aaltonen, I., Lahti, M., Engström, J., Mattila, J., Paananen, M., Paulamäki, S., Gehör, S., Kärki, A., Ahokas, T., Torvela, T. and Front, K.: Geological model of the Olkiluoto site, Version 2.0, Posiva Working Report 2010- 70, Posiva Oy, Eurajoki, 2010.

Aaltonen, I., Engström, J., Front, K., Gehör, S., Kosunen, P. and Kärki, A.: Geology of Olkiluoto. Posiva Working Report 2016- 16., Posiva Oy, Eurajoki., 2016.

Andersen, T., Austrheim, H. and Burke, E. A. J.: Fluid inclusions in granulites and eclogites from the Bergen Arcs, Caledonides of W. Norway, Mineral. Mag., 54, 145–158, 1990.

Ault, A. K. and Selverstone, J.: Microtextural constraints on the interplay between fluid-rock reactions and deformation, Contrib. to Mineral. Petrol., 156(4), 501–515, doi:10.1007/s00410-008-0298-9, 2008.

Bakker, R.: Re-Equilibration Processes in Fluid Inclusion Assemblages, Minerals, 7(7), 117, doi:10.3390/min7070117, 2017.

Bakker, R. J. and Jansen, J. B. H.: Preferential water leakage from fluid inclusions by means of mobile dislocations, Nature, 345(6270), 58–60, doi:10.1038/345058a0, 1990.

Bakker, R. J. and Jansen, J. B. H.: Experimental post-entrapment water loss from synthetic CO2-H2O inclusions in natural quartz, Geochim. Cosmochim. Acta, 55(8), 2215–2230, doi:10.1016/0016-7037(91)90098-P, 1991.

Bakker, R. J. and Jansen, J. B. H.: A mechanism for preferential H2O leakage from fluid inclusions in quartz, based on TEM observations, Contrib. to Mineral. Petrol., 116(1–2), 7–20, doi:10.1007/BF00310686, 1994.

Barton, P. B. and Bethke, P. M.: Chalcopyrite disease in sphalerite: Pathology and epidemiologyt, Am. Mineral., 72(5–6), 451–467, 1987.

Basson, I. J. and Viola, G.: Passive kimberlite intrusion into actively dilating dyke-fracture arrays: Evidence from fibrous

673   calcite veins and extensional fracture cleavage, Lithos, 76(1–4 SPEC. ISS.), 283–297, doi:10.1016/j.lithos.2004.03.041,
674   2004.

675   Bestmann, M., Pennacchioni, G., Nielsen, S., Göken, M. and de Wall, H.: Deformation and ultrafine dynamic
676   recrystallization of quartz in pseudotachylyte-bearing brittle faults: A matter of a few seconds, J. Struct. Geol., 38, 21–38,
677   doi:10.1016/j.jsg.2011.10.001, 2012.

678   Bodnar, R. J.: The origin of fluid inclusions, in: Samson, I., Anderson, A. & Marshall, D. (eds.) Fluid inclusions:
679   Analysis and Interpretation. Vancouver, Canada: Mineralogical Association of Canada, 11-18, 2003a.

680   Bodnar, R. J.: Re-equilibration of fluid inclusions, in: Samson, I., Anderson, A. & Marshall, D. (eds.) Fluid inclusions:
681   Analysis and Interpretation. Vancouver, Canada: Mineralogical Association of Canada, 213-230, 2003b.

682   Bons, P. D.: The formation of large quartz veins by rapid ascent of fluids in mobile hydrofractures, Tectonophysics,
683   336(1–4), 1–17, doi:10.1016/S0040-1951(01)00090-7, 2001.

684   Bons, P. D., Elburg, M. A. and Gomez-Rivas, E.: A review of the formation of tectonic veins and their microstructures, J.
685   Struct. Geol., 43, 33–62, doi:10.1016/j.jsg.2012.07.005, 2012.

686   Boullier, A. M.: Fluid inclusions: Tectonic indicators, J. Struct. Geol., 21(8–9), 1229–1235, doi:10.1016/S0191-
687   8141(99)00039-5, 1999.

688   Bourdelle, F. and Cathelineau, M.: Low-temperature chlorite geothermometry: a graphical representation based on a a T−
689   R2+−Si diagram, Eur. J. Mineral., 27(5), 617–626, doi:10.1127/ejm/2015/0027-2467, 2015.

690   Caine, J. S., Evans, J. P. and Forster, C. B.: Fault zone architechture and permeability structure, Geology, 24(11), 1025–
691   1028, doi:10.1130/0091-7613(1996)024<1025, 1996.

692   Compton, K. E., Kirkpatrick, J. D. and Holk, G. J.: Cyclical shear fracture and viscous flow during transitional ductile-
693   brittle deformation in the Saddlebag Lake Shear Zone, California, Tectonophysics, 708, 1–14,
694   doi:10.1016/j.tecto.2017.04.006, 2017.

695   Cox, S. F.: Faulting processes at high fluid pressures: An example of fault valve behavior from the Wattle Gully Fault,
696   Victoria, Australia, J. Geophys. Res., 100(B7), 841–859, 1995.

697   Cox S. F.: Coupling between deformation, fluid pressures and fluid flow in ore-producing hydrothermal environments,
698   Econ. Geol., 100th Anniversary Volume, 39–75, 2005.

699   Cox, S. F.: Injection-driven swarm seismicity and permeability enhancement: Implications for the dynamics of
700   hydrothermal ore systems in high fluid-flux, overpressured faulting regimes - An invited paper, Econ. Geol., 111(3),
701   559–587, doi:10.2113/econgeo.111.3.559, 2016.

702   Cox, S., Knackstedt, M., & Braun, J.: Principles of structural control on permeability and fluid flow in hydrothermal
703   systems, Reviews in Econ. Geol., 14, 1-24, 2001.

704   Crider, J. G. and Peacock, D. C. P.: Initiation of brittle faults in the upper crust: A review of field observations, J. Struct.
705   Geol., 26(4), 691–707, doi:10.1016/j.jsg.2003.07.007, 2004.

706 De Paola, N., Collettini, C., Trippetta, F., Barchi, M. R. and Minelli, G.: A mechanical model for complex fault patterns
707 induced by evaporite dehydration and cyclic changes in fluid pressure, J. Struct. Geol., 29(10), 1573–1584,
708 doi:10.1016/j.jsg.2007.07.015, 2007.

709 Derez, T., Pennock, G., Drury, M. and Sintubin, M.: Low-temperature intracrystalline deformation microstructures in
710 quartz, J. Struct. Geol., 71, 3–23, doi:10.1016/j.jsg.2014.07.015, 2015.

711 Diamond, L. W.: Introduction to gas-bearing, aqueous fluid inclusions, in : Fluid Inclusions: Analysis and Interpretation,
712 edited by: I. Samson, A. Anderson, D. Marshall, eds., 363–372., 2003.

713 Diamond, L. W., Tarantola, A. and Stünitz, H.: Modification of fluid inclusions in quartz by deviatoric stress. II:
714 Experimentally induced changes in inclusion volume and composition, Contrib. to Mineral. Petrol., 160(6), 845–864,
715 doi:10.1007/s00410-010-0510-6, 2010.

716 Dubessy, J., Buschaert, S., Lamb, W., Pironon, J. and Thiéry, R.: Methane-bearing aqueous fluid inclusions: Raman
717 analysis, thermodynamic modelling and application to petroleum basins, Chem. Geol., 173(1–3), 193–205,
718 doi:10.1016/S0009-2541(00)00275-8, 2001.

719 Ehlers, C., Lindroos, A. and Selonen, O.: The late Svecofennian granite-migmatite zone of southern Finland-a belt of
720 transpressive deformation and granite emplacement., Precambrian Res., 64(1–4), 295–309, 1993.

721 Fall, A., Donald, R. and Bodnar, R. J.: The effect of fluid inclusion size on determination of homogenization temperature
722 and density of liquid-rich aqueous inclusions, Am. Mineral., 94(11–12), 1569–1579, doi:10.2138/am.2009.3186, 2009.

723 Garofalo, P. S.: Mass transfer during gold precipitation within a vertically extensive vein network (Sigma deposit -
724 Abitibi greenstone belt - Canada). Part II. Mass transfer calculations, Eur. J. Mineral., 16(5), 761–776, doi:10.1127/0935-
725 1221/2004/0016-0761, 2004.

726 Garofalo, P. S., Matthäi, S. K. & Heinrich, C. A.: Three-dimensional geometry, ore distribution, and time-integrated
727 mass transfer through the quartz-tourmaline-gold vein network of the Sigma deposit (Abitibi belt - Canada), Geofluids, 2,
728 217-232, 2002.

729 Garofalo, P. S., Fricker, M. B., Günther, D., Bersani, D. and Lottici, P.: Physical-chemical properties and metal budget of
730 Au-transporting hydrothermal fluids in orogenic deposits, Geol. Soc. London, Spec. Publ., 402(1), 71–102,
731 doi:10.1144/SP402.8, 2014.

732 Goddard, J. V. and Evans, J. P.: Chemical changes and fluid-rock interaction in faults of crystalline thrust sheets,
733 northwestern Wyoming, U.S.A., J. Struct. Geol., 17(4), 533–547, doi:10.1016/0191-8141(94)00068-B, 1995.

734 Goldstein, R. H. and Reynolds, T. J.: Fluid Inclusion Microthermometry, Syst. Fluid Inclusions Diagenetic Miner., 87–
735 121, doi:10.2110/scn.94.31.0087, 1994.

736 Gorbatschev, R. and Bogdanova, S.: Frontiers in the Baltic Shield, Precambrian Res., 64(1–4), 3–21, doi:10.1016/0301-
737 9268(93)90066-B, 1993.

738 Griffith, A. A.: The Phenomena of Rupture and Flow in Solids, Philos. Trans. R. Soc. london, 221(582–893), 163–198,
739 1920.

740 Guermani, A. and Pennacchioni, G.: Brittle precursors of plastic deformation in a granite: An example from the Mont
741 Blanc massif (Helvetic, western Alps), J. Struct. Geol., 20(2–3), 135–148, doi:10.1016/S0191-8141(97)00080-1, 1998.

742 Healy, J. H., Rubey, W. W., Griggs, D. T. and Raleigh, C. B.: The Denver Earthquakes. Disposal of waste fluids by
743 injection into a deep well has riggered earthquakes near Denver, Colorado., Science, 161(3848), 1301–1310, 1968.

744 Heinrich, C. A., Andrew, A. S., and Knill, M. D.: Regional metamorphism and ore formation: Evidence from stable
745 isotopes and other fluid tracers, Reviews in Econ Geol, 11, 97–117, 2000.

746 Kaduri, M., Gratier, J. P., Renard, F., Çakir, Z. and Lasserre, C.: The implications of fault zone transformation on
747 aseismic creep: Example of the North Anatolian Fault, Turkey, J. Geophys. Res. Solid Earth, 122(6), 4208–4236,
748 doi:10.1002/2016JB013803, 2017.

749 Kerrich, R.: Some effects of tectonic recrystallisation on fluid inclusions in vein quartz, Contrib. to Mineral. Petrol.,
750 59(2), 195–202, doi:10.1007/BF00371308, 1976.

751 Kjøll, H. J., Viola, G., Menegon, L. and Sørensen, B. E.: Brittle-viscous deformation of vein quartz under fluid-rich
752 lower greenschist facies conditions, Solid Earth, 6(2), 681–699, doi:10.5194/se-6-681-2015, 2015.

753 Kohlstedt, D. L., Evans, B. and Mackwell, S. J.: Strength of the lithosphere: Constraints imposed by laboratory
754 experiments, J. Geophys. Res., 100(B9), 587–602, 1995.

755 Korja, A., Heikkinen, P. and Aaro, S.: Crustal structure of the northern Baltic Sea palaeorift, Tectonophysics, 331(4),
756 341–358, doi:10.1016/S0040-1951(00)00290-0, 2001.

757 Kukkonen, I. T. and Lauri, L. S.: Modelling the thermal evolution of a collisional Precambrian orogen: High heat
758 production migmatitic granites of southern Finland, Precambrian Res., 168(3–4), 233–246,
759 doi:10.1016/j.precamres.2008.10.004, 2009.

760 Lahtinen, R. and Survey, G.: Palaeoproterozoic tectonic evolution of the Fennoscandian Shield. In: Lehtinen, M., Nurmi,
761 P.A., Rämö (eds.), Precambrian Geology of Finland: Key to the Evolution of the Fennoscandian Shield, Developments in
762 Precambrian Geology, 2005.

763 Mancktelow, N. S. and Pennacchioni, G.: The control of precursor brittle fracture and fluid-rock interaction on the
764 development of single and paired ductile shear zones, J. Struct. Geol., 27(4), 645–661, doi:10.1016/j.jsg.2004.12.001,
765 2005.

766 Mattila, J. and Viola, G.: New constraints on 1.7Gyr of brittle tectonic evolution in southwestern Finland derived from a
767 structural study at the site of a potential nuclear waste repository (Olkiluoto Island), J. Struct. Geol., 67(PA), 50–74,
768 doi:10.1016/j.jsg.2014.07.003, 2014.

769 Menegon, L., Pennacchioni G., Malaspina N., Harris K., and Wood E.: Earthquakes as Precursors of Ductile Shear Zones
770 in the Dry and Strong Lower Crust, Geochem. Geophy. Geosy., 18(12), doi: 10.1002/2015GC006010, 2017.

771 Menegon, L., Marchesini, B., Prando, F., Garofalo, P. S., Viola, G., Anderson, M.and Mattila, J.: Brittle-viscous
772 oscillations and different slip behaviours in a conjugate set of strike-slip faults, Geophysical Research Abstracts Vol. 20,
773 EGU2018-14799, 2018.

774   Miller, S. A.: The Role of Fluids in Tectonic and Earthquake Processes, edited by R. Dmowska, Elsevier., 2013.

775   Mittempergher, S., Dallai, L., Pennacchioni, G., Renard, F. and Di Toro, G.: Origin of hydrous fluids at seismogenic
776   depth: Constraints from natural and experimental fault rocks, Earth Planet. Sci. Lett., 385, 97–109,
777   doi:10.1016/j.epsl.2013.10.027, 2014.

778   Nekrasov, I. J., Sorokin, V. I. and Osadchii, E. G.: Fe and Zn partitioning between stannite and sphalerite and its
779   application in geothermometry., Phys. Chem. Earth, 11(C), 739–742, doi:10.1016/0079-1946(79)90069-7, 1979.

780   Oliver, N. H. S. and Bons P. D.: Mechanisms of fluid flow and fluid–rock interaction in fossil metamorphic hydrothermal
781   systems inferred from vein–wallrock patterns, geometry and microstructure, Geofluids, 137–162, 2001.

782   Olsen, M. P., Scholz, C. H. and Léger, A.: Healing and sealing of a simulated fault gouge under hydrothermal conditions:
783   Implications for fault healing, J. Geophys. Res., 103(B4), 7421, doi:10.1029/97JB03402, 1998.

784   Passchier, C. W. and Trouw, R. A. J.: Microtectonics, 2nd edition. Berlin: Springer, 2005.

785   Pennacchioni, G., Di Toro, G., Brack, P., Menegon, L. and Villa, I. M.: Brittle-ductile-brittle deformation during cooling
786   of tonalite (Adamello, Southern Italian Alps), Tectonophysics, 427(1–4), 171–197, doi:10.1016/j.tecto.2006.05.019,
787   2006.

788   Roedder, E. and Bodnar, R. J.: Geologic determinations from fluid inclusion studies., Annu. Rev. Earth Planet. Sci.,
789   8(1953), 263–301, 1980.

790   Rolandone, F. and Jaupart, C.: The distributions of slip rate and ductile deformation in a strike-slip shear zone, Geophys.
791   J. Int., 148(2), 179–192, doi:10.1046/j.1365-246X.2002.01574.x, 2002.

792   Rosso, K. M. and Bodnar, R. J.: Microthermometric and Raman spectroscopic detection limits of CO_2 in fluid inclusions
793   and the Raman spectroscopic characterization of CO_2, Geochim. Cosmochim. Acta, 59(19), 3961–3975,
794   doi:10.1016/0016-7037(95)94441-H, 1995.

795   Scholz, C. H.: The Mechanics of Earthquakes and Faulting, Cambridge: Cambridge University Press, 1990.

796   Shimizu, M. and Shikazono, N.: Mineralium deposita ©, Miner. Depos., 20, 314–320, 1985.

797   Sibson, R. H.: A note on fault reactivation, J. Struct. Geol., 7(6), 751–754, doi:10.1016/0191-8141(85)90150-6, 1985.

798   Sibson, R. H.: Earthquake faulting as a structural process, J. Struct. Geol., 11(1–2), 1–14, doi:10.1016/0191-
799   8141(89)90032-1, 1989.

800   Sibson, R. H.: Fault-valve behavior and the hydrostatic-lithostatic fluid pressure interface, Earth Sci. Rev., 32(1–2), 141–
801   144, doi:10.1016/0012-8252(92)90019-P, 1992a.

802   Sibson, R. H.: Implications of fault-valve behaviour for rupture nucleation and recurrence., Tectonophysics, 211(1–4),
803   283–293., 1992b.

804   Sibson, R. H.: Load-strengthening versus load-weakening faulting, J. Struct. Geol., 15(2), 123–128, doi:10.1016/0191-

805   8141(93)90090-W, 1993.

806   Sibson, R. H.: Structural permeability of fluid-driven fault-fracture meshes-Sibson-J Struct Geol-1996.pdf, , 18(8), 1996.

807   Sibson, R. H., Robert, F. and Poulsen, K. H.: High-angle reverse faults, fluid-pressure cycling, and mesothermal gold-
808   quartz deposits, , 16(June 1988), 551–555, doi:10.1130/0091-7613(1988)016<0551:HARFFP>2.3.CO;2, 1988.

809   Siebenaller, L., Vanderhaeghe, O., Jessell, M., Boiron, M. C. and Hibsch, C.: Syntectonic fluids redistribution and
810   circulation coupled to quartz recrystallization in the ductile crust (Naxos Island, Cyclades, Greece), J. Geodyn., 101,
811   129–141, doi:10.1016/j.jog.2016.07.001, 2016.

812   Skyttä, P. and Torvela, T.: Brittle reactivation of ductile precursor structures: The role of incomplete structural
813   transposition at a nuclear waste disposal site, Olkiluoto, Finland, J. Struct. Geol., 0–1, doi:10.1016/j.jsg.2018.06.009,
814   2018.

815   Spruzeniece, L. and Piazolo, S.: Strain localization in brittle-ductile shear zones: Fluid-abundant vs. fluid-limited
816   conditions (an example from Wyangala area, Australia), Solid Earth, 6(3), 881–901, doi:10.5194/se-6-881-2015, 2015.

817   Steele-MacInnis, M., Lecumberri-Sanchez, P. and Bodnar, R. J.: HokieFlincs_H2O-NaCl: A Microsoft Excel spreadsheet
818   for interpreting microthermometric data from fluid inclusions based on the PVTX properties of H_2O-NaCl, Comput.
819   Geosci., 49, 334–337, doi:10.1016/j.cageo.2012.01.022, 2012.

820   Sterner, S. M. and Bodnar J.: Synthetic fluid inclusions - VII. Re-equilibration of fluid inclusions in quartz during
821   laboratory-simulated metamorphic burial and uplift, J. Metamorph. Geol., 7, 243–260, 1989.

822   Suominen, V.: The chronostratigraphy of southern Finland, with special reference to Postjotnian and Subjotnian diabases.
823   Bull. Geol. Surv. Finl,. 356, 100, 1991.

824   Tarantola, A., Diamond, L. W. and Stünitz, H.: Modification of fluid inclusions in quartz by deviatoric stress I:
825   Experimentally induced changes in inclusion shapes and microstructures, Contrib. to Mineral. Petrol., 160, 825–843,
826   doi:10.1007/s00410-010-0509-z, 2010.

827   Tchalenko, J. S.: Similarities between Shear Zones of Different Magnitudes, Geol. Soc. Am. Bull., 81(6), 1625–1640,
828   doi:10.1130/0016-7606(1970)81[1625:SBSZOD]2.0.CO;2, 1970.

829   Tenthorey, E. and Cox, S. F.: Cohesive strengthening of fault zones during the interseismic period: An experimental
830   study, J. Geophys. Res. Solid Earth, 111(9), 1–14, doi:10.1029/2005JB004122, 2006.

831   Trepmann, C. A. and Stöckhert, B.: Quartz microstructures developed during non-steady state plastic flowat rapidly
832   decaying stress and strain rate, J. Struct. Geol., 25(12), 2035–2051, doi:10.1016/S0191-8141(03)00073-7, 2003.

833   Trepmann, C. A. and Stöckhert, B.: Short-wavelength undulatory extinction in quartz recording coseismic deformation in
834   the middle crust – An experimental study, Solid Earth, 4(2), 263–276, doi:10.5194/se-4-263-2013, 2013.

835   Trepmann, C. A., Stöckhert, B., Dorner, D., Moghadam, R. H., Küster, M. and Röller, K.: Simulating coseismic
836   deformation of quartz in the middle crust and fabric evolution during postseismic stress relaxation - An experimental
837   study, Tectonophysics, 442(1–4), 83–104, doi:10.1016/j.tecto.2007.05.005, 2007.

838 Trepmann, C. A., Hsu, C., Hentschel, F., Döhler, K., Schneider, C. and Wichmann, V.: Recrystallization of quartz after
839 low-temperature plasticity – The record of stress relaxation below the seismogenic zone, J. Struct. Geol., 95, 77–92,
840 doi:10.1016/j.jsg.2016.12.004, 2017.

841 van den Kerkhof, A., Kronz, A. and Simon, K.: Deciphering fluid inclusions in high-grade rocks, Geosci. Front., 5(5),
842 683–695, doi:10.1016/j.gsf.2014.03.005, 2014.

843 Viola, G., Mancktelow, N. S. and Miller, J. A.: Cyclic frictional-viscous slip oscillations along the base of an advancing
844 nappe complex: Insights into brittle-ductile nappe emplacement mechanisms from the Naukluft Nappe Complex, central
845 Namibia, Tectonics, 25(3), 1–20, doi:10.1029/2005TC001939, 2006.

846 Viola, G., Venvik Ganerød, G. and Wahlgren, C. H.: Unraveling 1.5 Ga of brittle deformation history in the Laxemar-
847 Simpevarp area, southeast Sweden: A contribution to the Swedish site investigation study for the disposal of highly
848 radioactive nuclear waste, Tectonics, 28(5), 1–29, doi:10.1029/2009TC002461, 2009.

849 Viola, G., Mattila, J., Zwingmann, H., Todd, A. and Raven, M.: Structural and K / Ar Illite Geochronological Constraints
850 on the Brittle Deformation History of the Olkiluoto Region , Southwest Finland Structural and K / Ar Illite
851 Geochronological Constraints on the Brittle Deformation History of the Olkiluoto Region , 2011.

852 Viola, G., Scheiber, T., Fredin, O., Zwingmann, H., Margreth, A. and Knies, J.: Deconvoluting complex structural
853 histories archived in brittle fault zones, Nat. Commun., 7, 1–10, doi:10.1038/ncomms13448, 2016.

854 Vityk, M. O. and Bodnar, R. J.: Textural evolution of synthetic fluid inclusions in quartz during reequilibration, with
855 applications to tectonic reconstruction, Contrib. to Mineral. Petrol., 121(3), 309–323, doi:10.1007/BF02688246, 1995.

856 Vityk, M. O. and Bodnar, R. J.: Statistical microthermometry of synthetic fluid inclusions in quartz during
857 decompression reequilibration, Contrib. to Mineral. Petrol., 132(2), 149–162, doi:10.1007/s004100050413, 1998.

858 Vityk, M. O., Bodnar, R. J. and Schmidt, C. S.: Fluid inclusion as a tectonothermobarometers: Relation between
859 pressure-tempreture history and reequilibration morphology during crystal thickening, Geology, 22, 731–734,
860 doi:10.1130/0091-7613(1994)022<0731:FIATRB>2.3.CO, 1994.

861 Wehrens, P., Berger, A., Peters, M., Spillmann, T. and Herwegh, M.: Deformation at the frictional-viscous transition:
862 Evidence for cycles of fluid-assisted embrittlement and ductile deformation in the granitoid crust, Tectonophysics, 693,
863 66–84, doi:10.1016/j.tecto.2016.10.022, 2016.

864 Wilkins, R. W. T. and Barkas, J. P.: Geological History and its Impact on the Rock Mechanics Properties of the Olkiluoto
865 Site. Working Report 2006-14, Contrib. to Mineral. Petrol., 65, 293–299, 1978.

866

867

868

869
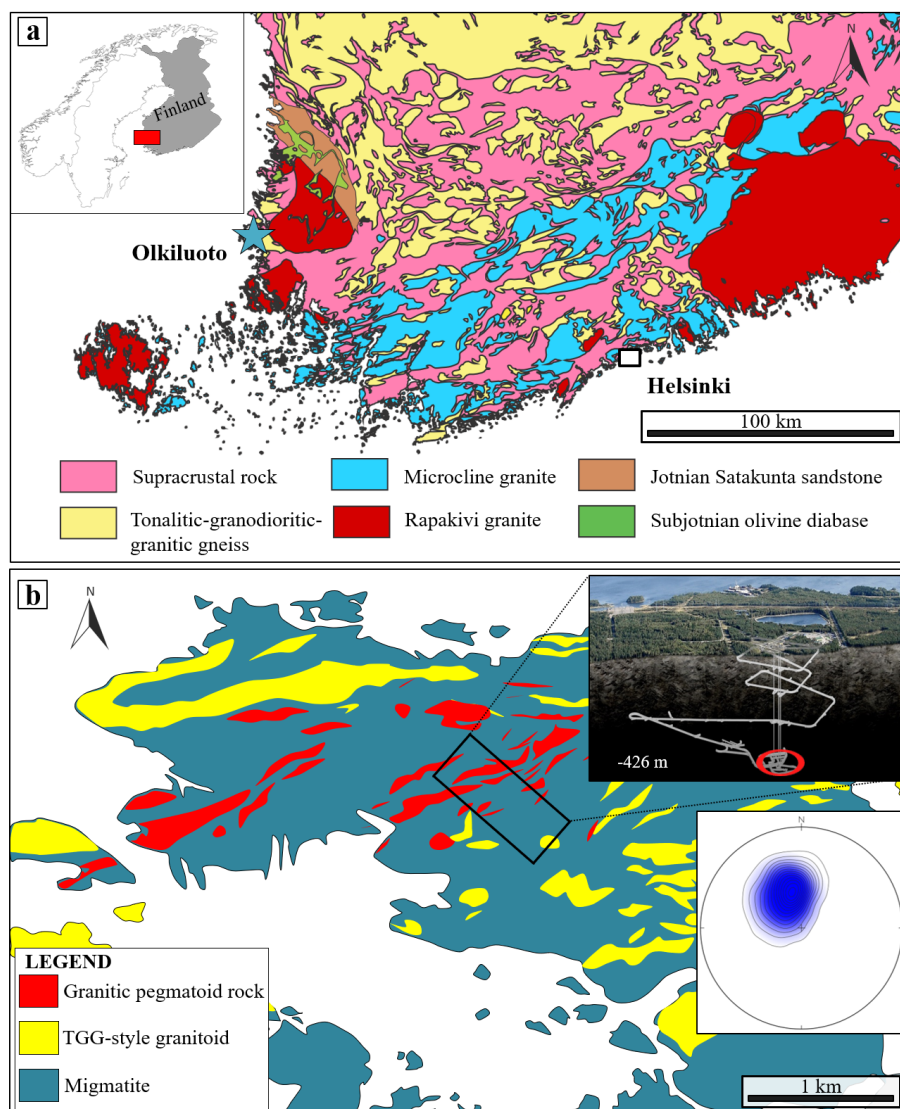
Figure 1. (a) Simplified geological map of Southern Finland Subprovince (modified after: Mattila and Viola 2014). (b) Geological sketch of the Olkiluoto site. The upper inset on the right is a panoramic photo with an overlay drawing of the underground infrastructure (photo: courtesy of Posiva Oy, Finland). The red circle shows the depth location of BFZ300. The lower inset on the right shows the poles to foliation planes measured from the Olkiluoto drill cores (Mattila and Viola, 2014). This is mainly low-angle and SE-dipping.

874
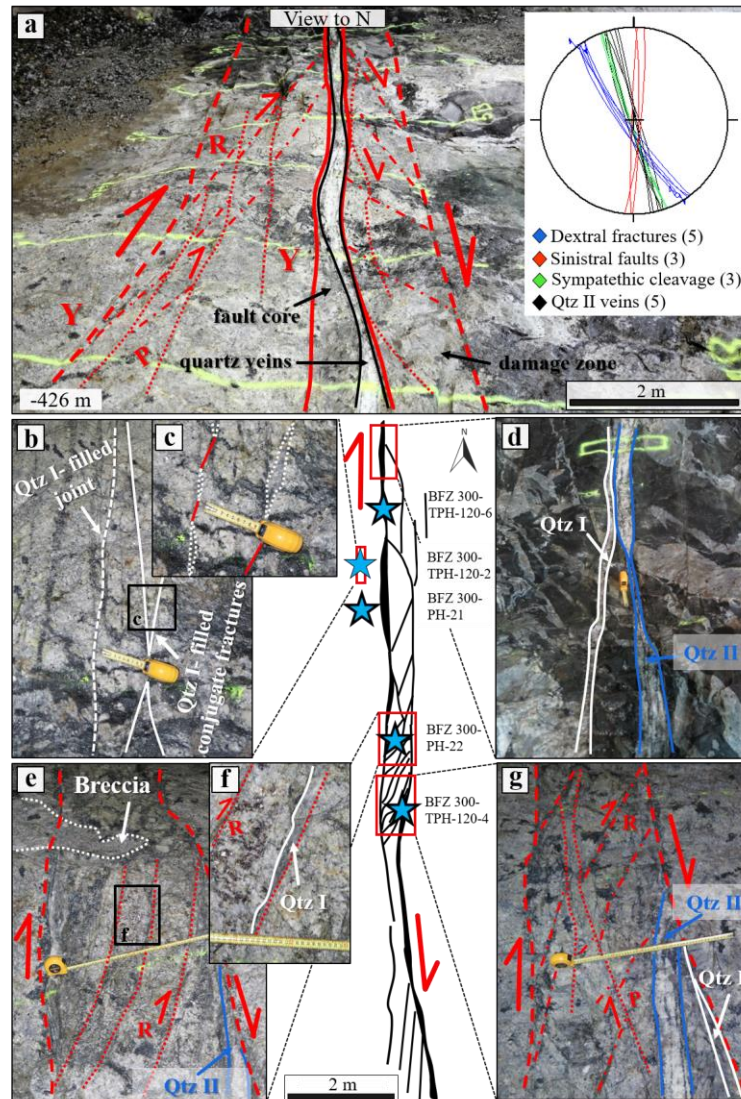
Figure 2. BFZ300 fault geometry and architecture (centre of figure) and examples of representative outcrop features. The red rectangles locate the areas along the fault segments where detailed outcrop photos were taken. Stars locate hand and drill core samples. Stars with black layout identifysamples used for the microthermometric study. Note that the fault is made of two segments offset laterally at a astep over zone with overall dextral kinematics. Fault core quartz veins are shown by thicker black lines in the schematic model. (a) View and interpretation of the structural elements of the fault, whose core hosts two generations of quartz-chlorite veins. Inset shows lower-hemisphere, equiangular projection of conjugate fault segments, cleavage and quartz-chlorite veins. (b) Damage zone made of mm-thick, en-echelon veins connected by conjugate shear segments. (c) Detail of (b) showing fractures filled by the first quartz generation (Qtz I). (d) Two distinct generations of quartz-chlorite veins recognised in the fault core (Qtz I and Qtz II). (e) Detail of the compressional step-over zone characterized by multiple and parallel T fractures, filled by Qtz I. A brecciated body is crosscut by the Y planes. (f) Detail of a Tensional fracture infilled by Qtz I. (g) Compressional structures (P shears) from the step-over zone and relationships between Qtz I and Qtz II within the fault. The Riedel geometry suggests that the Qtz II vein formed due to the reactivation of the principal slip zones..

886
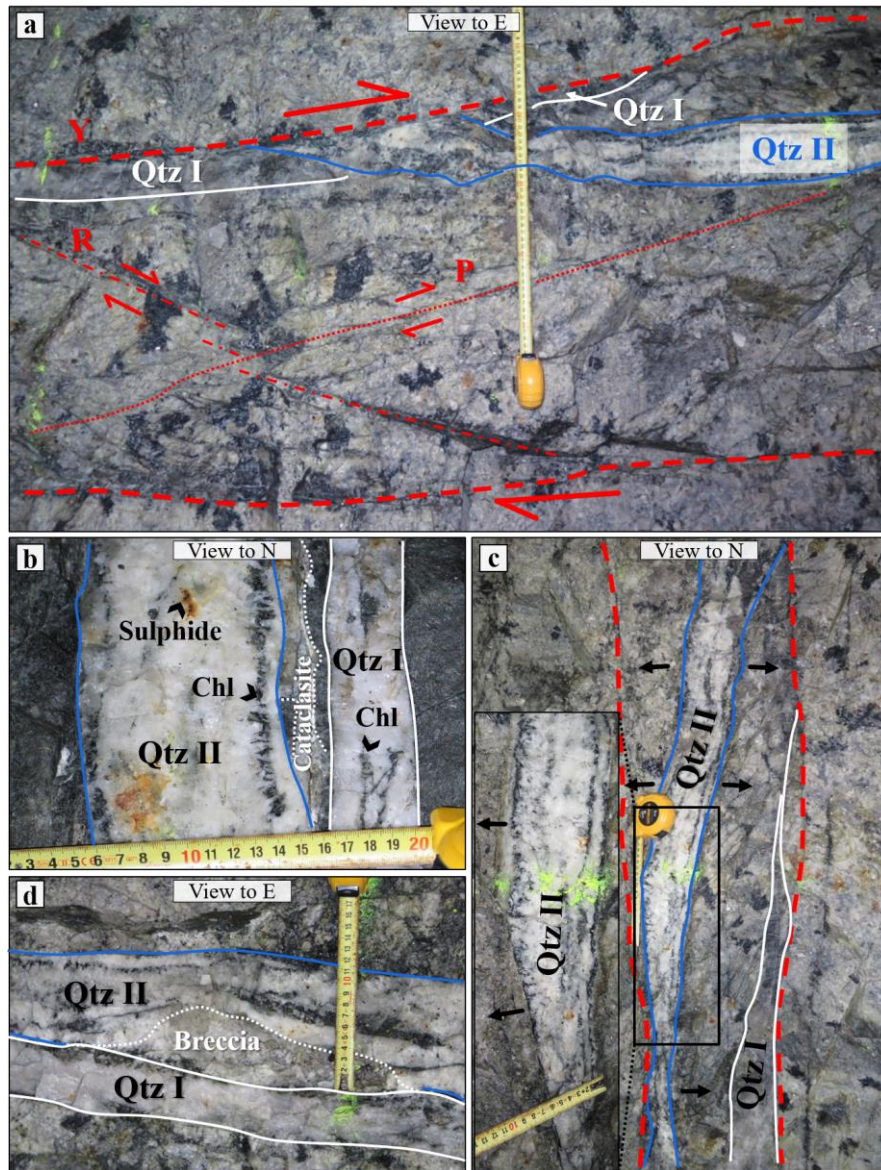
Figure 3. Relationships between Riedel shears and quartz-chlorite veins. (a) Sharp shear boundaries along fault veins and Riedel shears. The
geometry of the R and P shears suggests a dextral kinematics. White lines highlight the positions of the two types of quartz veins. Note the Qtz
II vein cutting the Qtz I vein. (b) Juxtaposed Qtz I and Qtz II veins. Qtz I veins are thinner and made of a translucid, small grained quartz. In
contrast, Qtz II veins, which contain pockets of sulphide aggregates, are thicker and made of larger and euhedral quartz. Chlorite occurs as
minor phase in both types of veins, but only in Qtz II veins it forms long and prismatic aggregates growing perpendicular to the fracture walls.
In Qtz I veins, chlorite is small grained and forms thin levels within the quartz. Notice the presence of a cataclastic band between the two
veins. (c) Spatial continuity of the chlorite aggregates within the Qtz II veins, which grow always orthogonal to the vein boundaries. Inset
shows the detail of the prismatic aggregates forming long and parallel ribbons. This open space filling texture suggests hybrid conditions of
reactivation of the older Qtz I veins. (d) Small quartz breccia formed between the two generations of quartz veins.

896
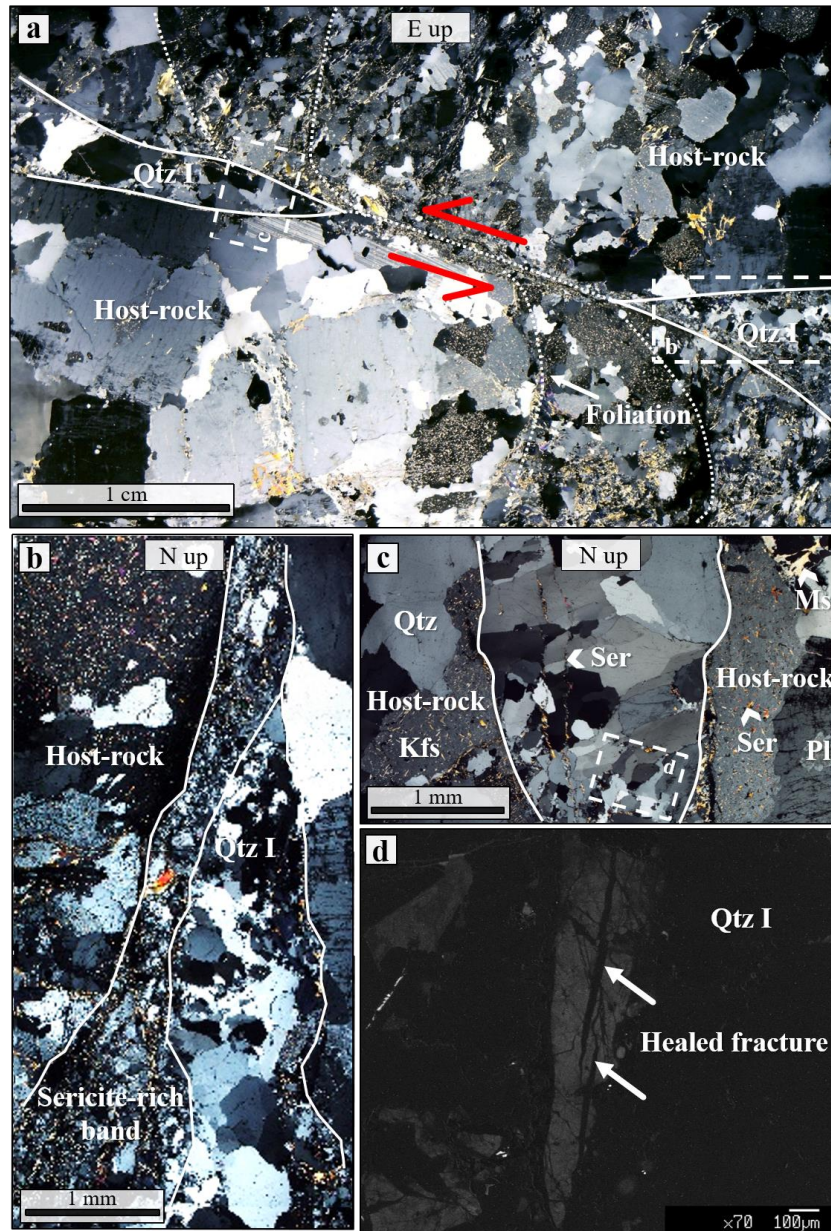
Figure 4. Microtextural characteristics of Qtz I from the damage zone of BFZ300 (sample: TPH-120-2). (a) Composition of photomicrographs of a Qtz I vein interconnecting with a sinistral shear band (crossed nicols). Faulting kinematics is suggested by drag folds in the host rock. (b) Tip of Qtz I vein hosted by a sericite-rich cataclastic band of the host rock. (c) Detail of panel a showing open-space filling texture in the Qtz I vein. Notice the sericite microfractures crosscutting Qtz I. (d) Panchromatic cathodoluminescence image of Qtz I showing healed microfractures crosscutting the crystal.

904
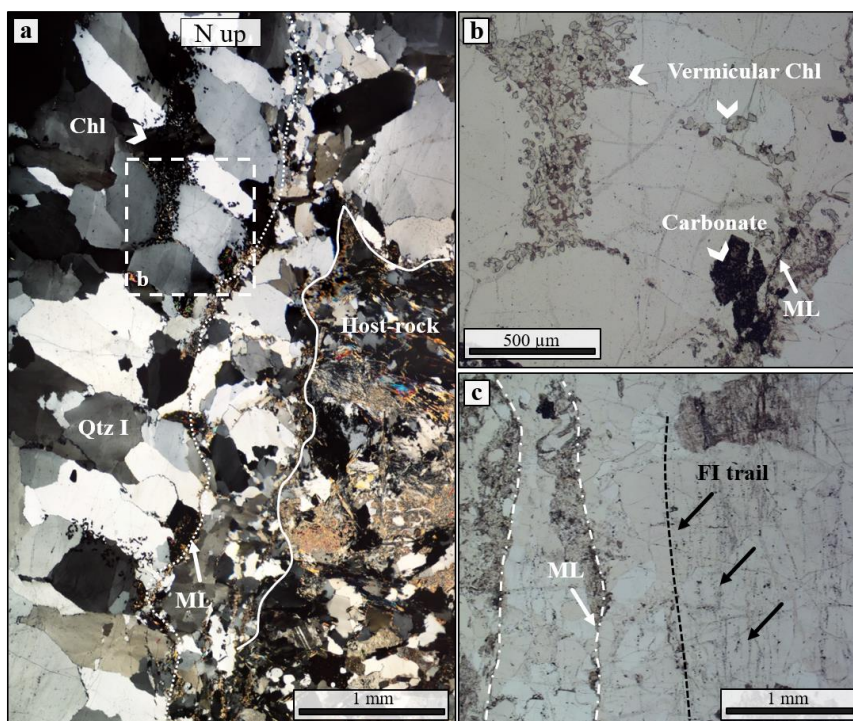
Figure 5. Microtextural characteristics of Qtz I from the damage zone of BFZ300 (sample PH-21). (a) Stitched microphotographs of a Qtz I vein showing elongated-blocky texture with crystals growing obliquely with respect to the vein boundaries, which suggests growth under oblique dilation. Mode I opening is highlighted by the presence of a median line (ML) that is decorated by syn-kinematic chlorite and aggregates of REE-bearing carbonate. (b) Detailed view of the chlorite and carbonate found along the ML. (c) Photomicrograph (plane polarized light) showing a set of fluid inclusion trails parallel to the median lines and crosscutting Qtz I, which suggests crack-seal opening and sealing.
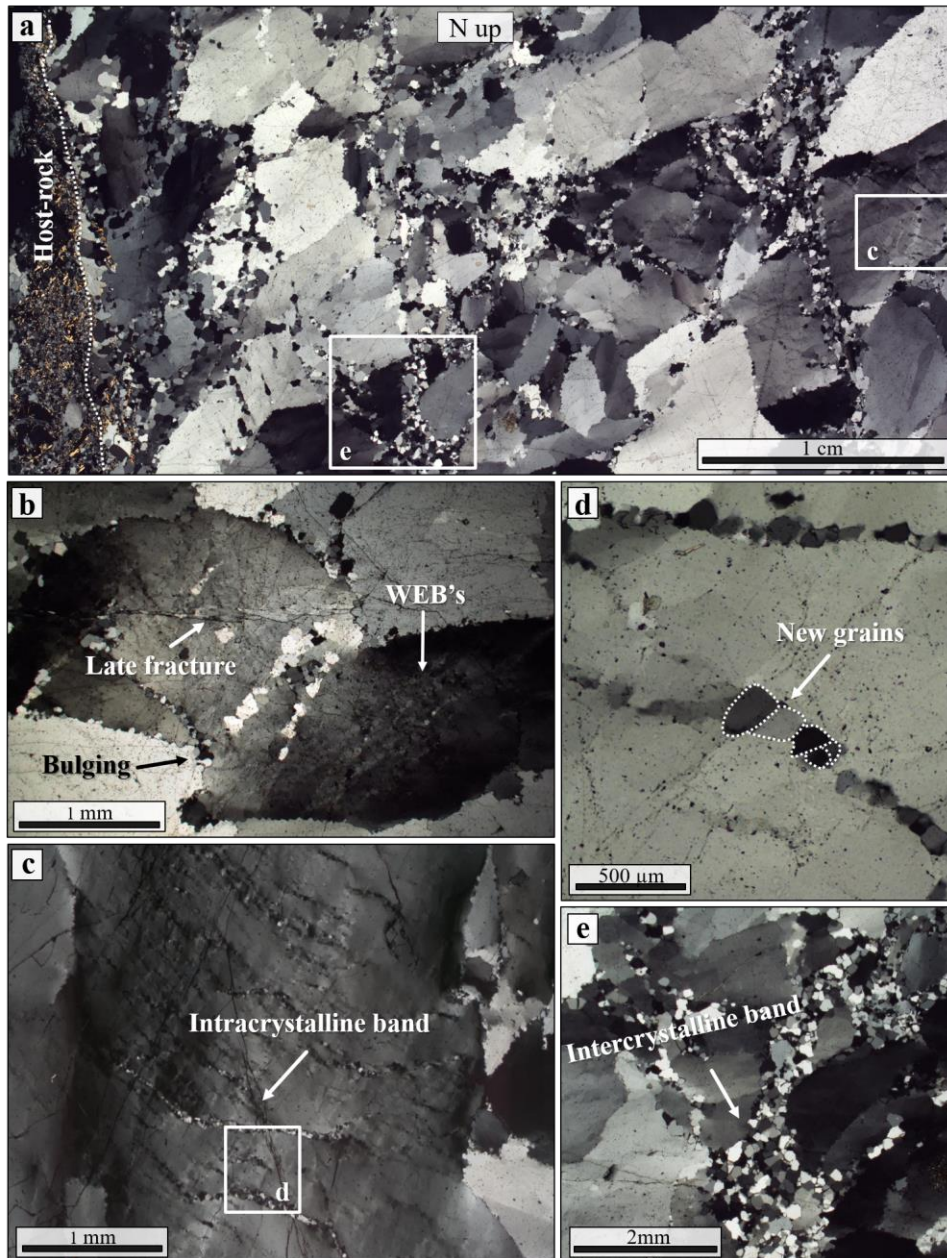
911
912 Figure 6. Microtextural characteristics of Qtz I from the BFZ300 core (sample TPH-120-4). (a) Stitched photomicrographs showing the typical
913 heterogeneous grain size of Qtz I (30-800 µm). (b) Evidence of plastic deformation of Qtz I from the fault core given by bulging of the largest
914 crystals, wide extinction bands and undulose extinction. Note the late brittle fractures crosscutting all the previously formed plastic features.
915 (c) Intracrystalline deformation bands within a large crystal. (d) Detail of (c) showing the typical grain size of the band (50-250 µm).
916 Intracrystalline deformation bands are oriented at <30° with respect to the BFZ300 vein walls and can be up to 2 mm in length. (e)
917 Intercrystalline deformation band showing a thickening at the triple junction of larger grains. These intercrystalline bands are parallel to the
918 strike of BFZ300.

919
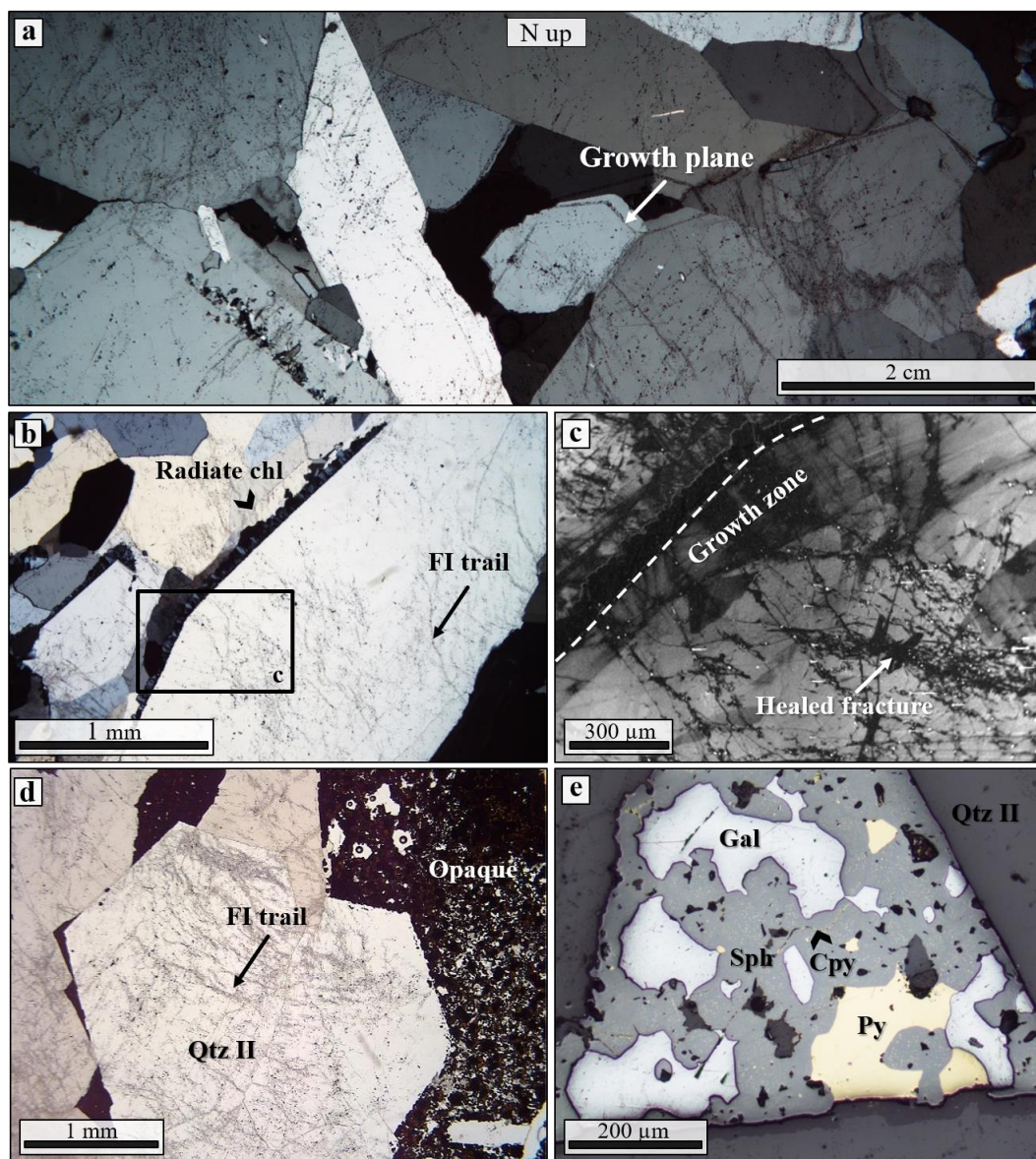
Figure 7. Microstructural characteristics of Qtz II from BFZ300 (samples TPH-120-6, PH-22). (a) Stitched photomicrographs of Qtz II vein from the fault core. Notice the coarse quartz crystals and their elongated-blocky texture. Primary growth textures are sometimes visible and are marked by solid inclusions and decrepitated FIAs. (b) Radiate chlorite crystals along a prismatic Qtz II crystal boundary. Note that Qtz II is crosscut by numerous trails of FIs. (c) Panchromatic cathodoluminescence image of the same large Qtz II crystal from panel b, showing radiate chlorite along the crystal boundary and a primary growth zone cut by a set of healed fractures. (d) Euhedral quartz crystals set within opaque phases and crosscut by a network of thin microfractures. (e) Reflected light photomicrograph showing the opaque mineral assemblage typically associated with Qtz II, i.e. subhedral to anhedral sphalerite, pyrite, and galena. Chalcopyrite is a minor phase and occurs as small round inclusions within sphalerite (chalcopyrite "disease") or as large subhedral/anhedral masses together with galena.
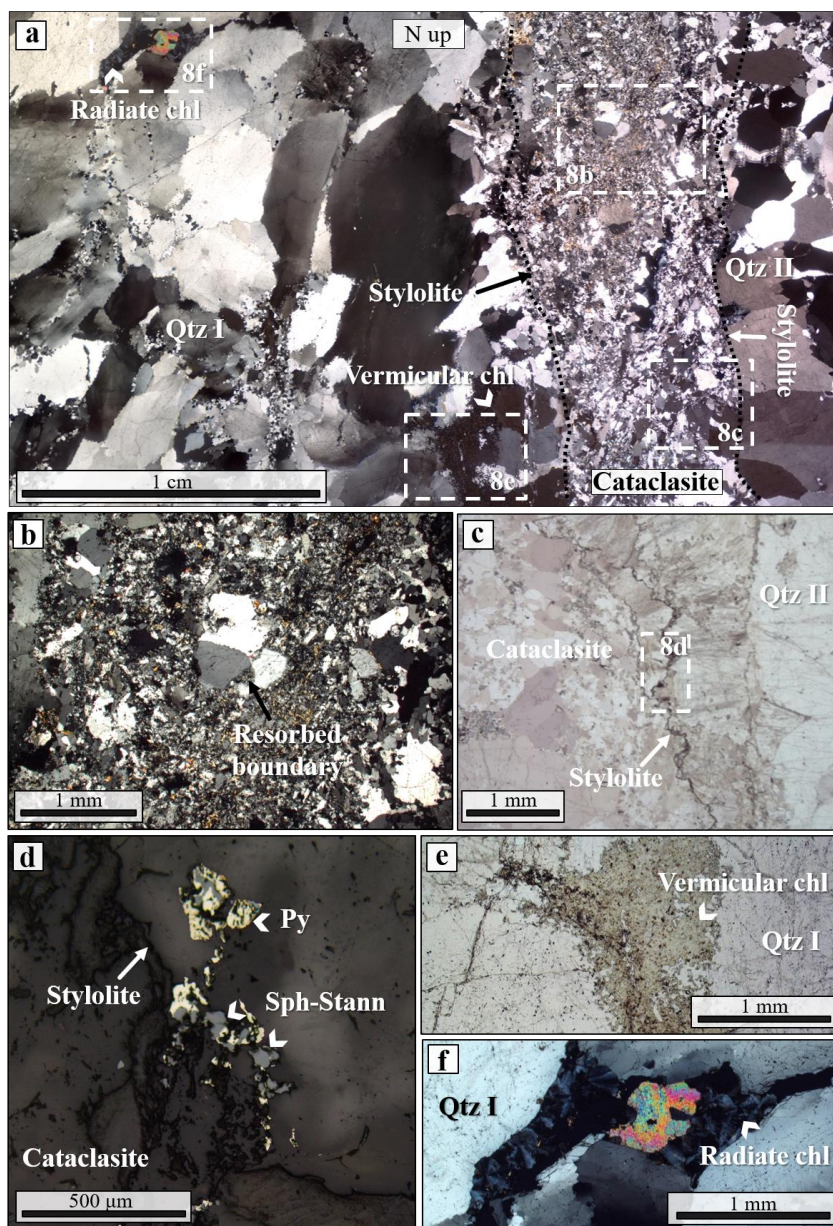
Figure 8. Microtextural characteristics of the cataclasite juxtaposing Qtz I and Qtz II veins (sample TPH-120-4). (a) Stitched photomicrographs covering the contact between the two quartz veins and the intervening, 5 mm-thick cataclastic band. (b) Cataclastic band made of large Qtz I fragments (8-12 mm) embedded within a finer matrix (20-200 µm in size) made of sericite and quartz. The largest crystals show lobate boundaries, suggesting dissolution and local resorption along the clast-matrix interface. (c) Detail view of the cataclastic band, which is defined by two stylolite seams that strike parallel to the BFZ300. (d) Reflected-light photomicrograph showing anhedral to subhedral pyrite, chalcopyrite, stannite, and sphalerite arranged along the stylolite as residual product of pressure solution. (e) Vermicular chlorite associated with Qtz I close to the cataclastic band. (f) Radiate chlorite associated with Qtz I.
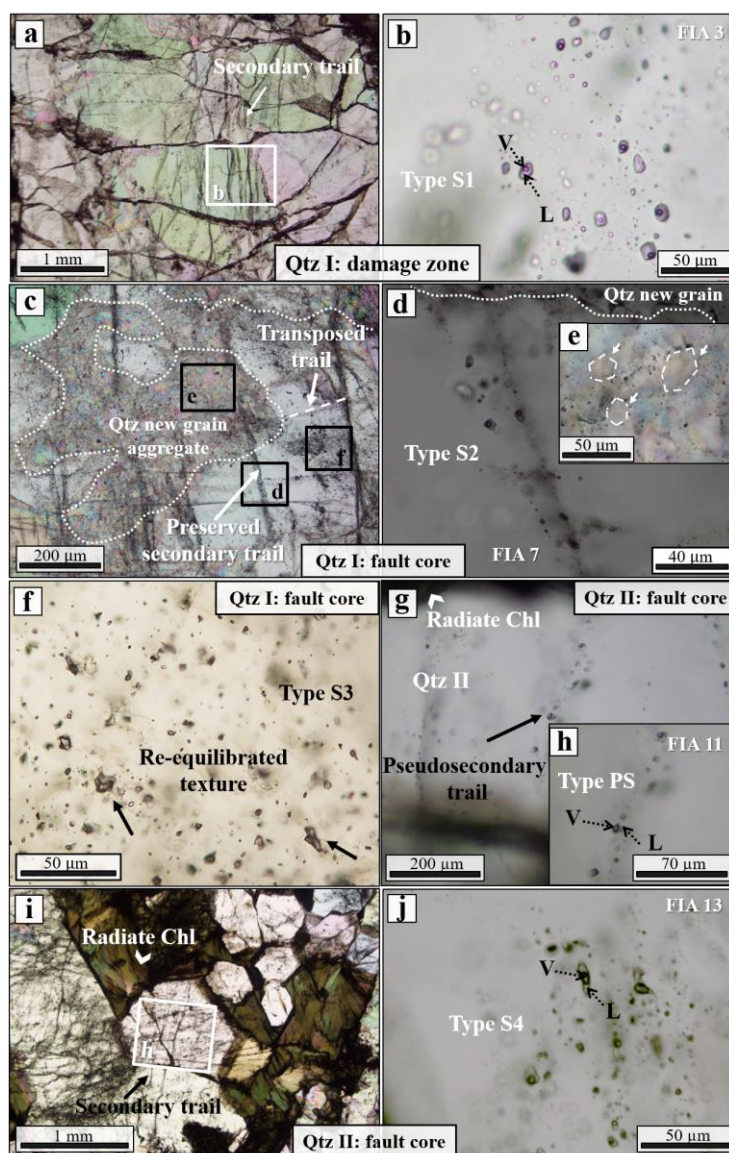
Figure 9. Characteristics textures of FIAs hosted within the BFZ300 quartz (samples PH-21, TPH-120-4, TPH-120-6). (a) Secondary trails crosscutting large Qtz I crystals of the damage zone. (b) Detail of (a) showing the phase ratios of one of the studied secondary assemblages (FIA3), most representative of Type S1 FIA. (c) Long secondary transgranular trails crosscutting Qtz I of the fault core, dismembered by intercrystalline fractures, infilled by quartz new grains. Qtz I fault core also hosts set of short sub-trails developed at high angle with respect to the long trails. (d) Detail of Type S2 FIA entrapped along a preserved secondary fracture trail. (e) Small inclusions (<1μm) arranged along the boundaries of new polygonal quartz. (f) Example of Type S3 FIA arranged as isolated clusters inside ductile deformed fault core Qtz I. These trails formed during a brittle deformation stage that pre-dates ductile re-crystallization. (g) Pseudosecondary FIA associated with Qtz II-chlorite (FIA11) and (h) its phase ratio details. (i) Small scale view of secondary FIAs crosscutting Qtz II. (j) Detail of secondary trails crosscutting euhedral Qtz II (FIA 13). In all photographs north points up.
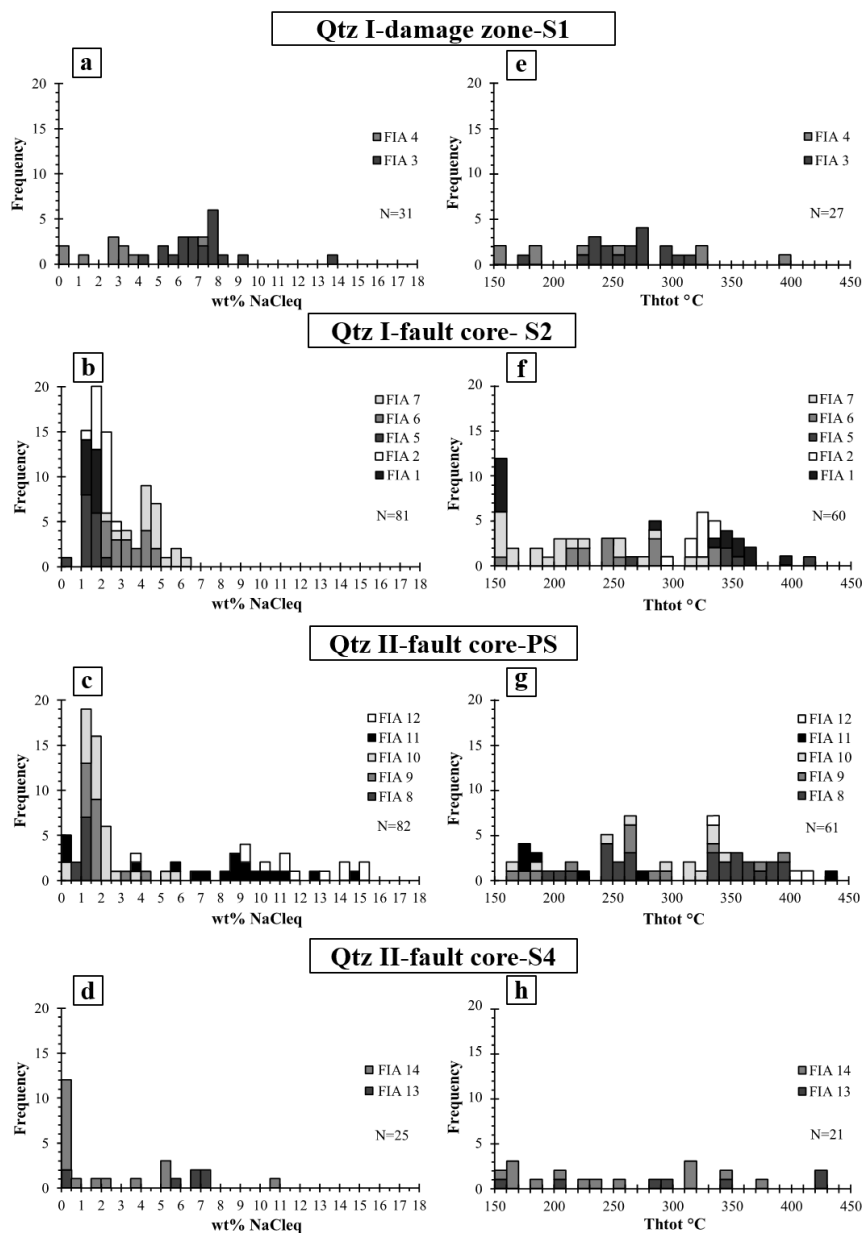
947
948 Figure 10. Microthermometric data of the studied FIAs. Panels a-d show the bulk salinities of individual FIAs calculated from the Tmice data
949 while panels e-h refer to the temperatures of final homogenization of the same assemblages. Notice that the data report the properties of
950 individual FIAs according to their occurrence within Qtz I of the damage zone, Qtz I from the fault core, and Qtz II from the fault core. Notice
951 that pseudosecondary (PS) and secondary (S) FIAs identify progressive later stages of fluid entrapment, and can be used to constrain the fluid
952 properties in the fault zone. Notice also that the measured ranges of Thtot spread across T intervals that are too large to represent entrapment at
953 equilibrium (e.g., FIA7 of Qtz I from fault core: 150-330 °C), which suggests post-entrapment re-equilibration of the inclusions. Fluid bulk
954 composition is expressed as salinity, which is conventionally reported as weight percent of NaCl equivalents (wt%NaCleq, Roedder,1984).
955

956
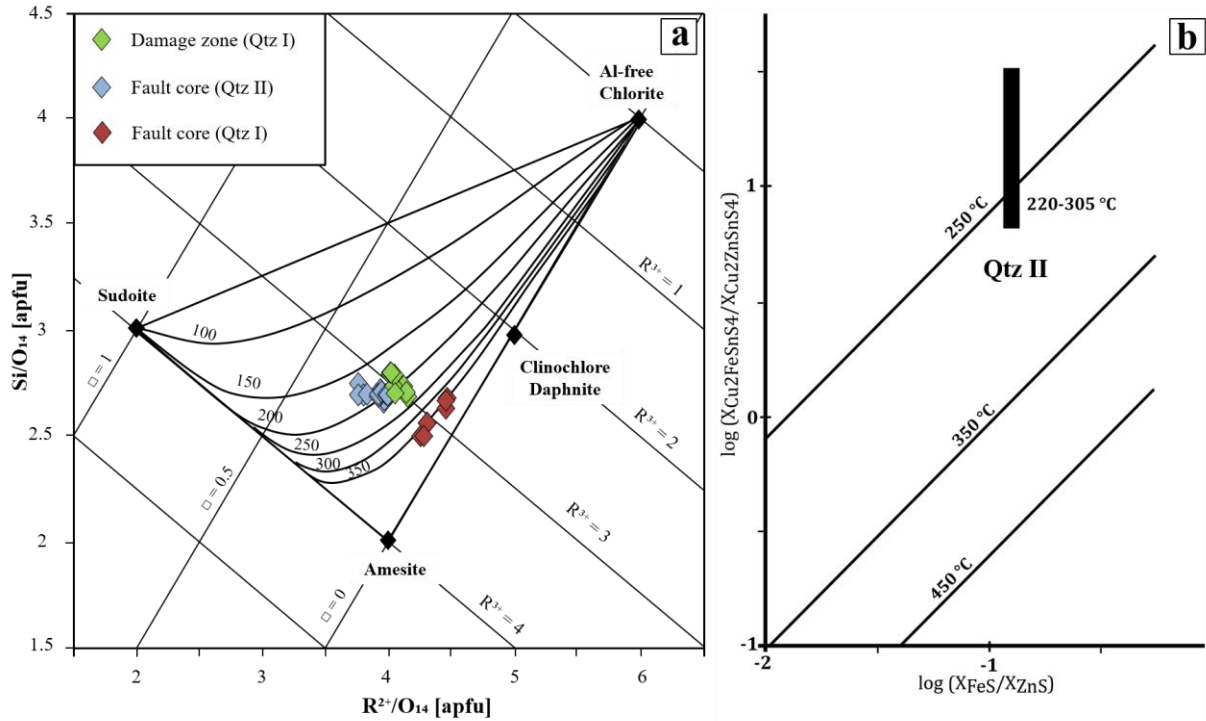
957

958 Figure 11. Mineral-pair geothermometry applied to the assemblages of the QtzI- and Qtz II veins. (a) Chlorite-quartz formation temperature
959 estimated using the method of Bourdelle and Cathelineau (2015). Green, red, and light blue symbols indicate the distinct textural types of
960 chlorite in Qtz I and II, respectively. The maximum temperature is from the Qtz I-chlorite pair from the fault core. The other groups of
961 chlorites in the 150-250 °C range indicate a second stage of quartz-chlorite precipitation in the fault core and damage zone, in line with
962 microthermometric constraints. (b) Temperature of sphalerite-stannite formation estimated with the method of Shimizu & Shikazono (1985)
963 that uses Fe and Zn partitioning between stannite and sphalerite. The region of the plot that was calibrated with this geothermometer lies
964 between the 250 and 450 °C isotherms. Hence, compositions corresponding to T<250 °C should be interpreted with caution.
965
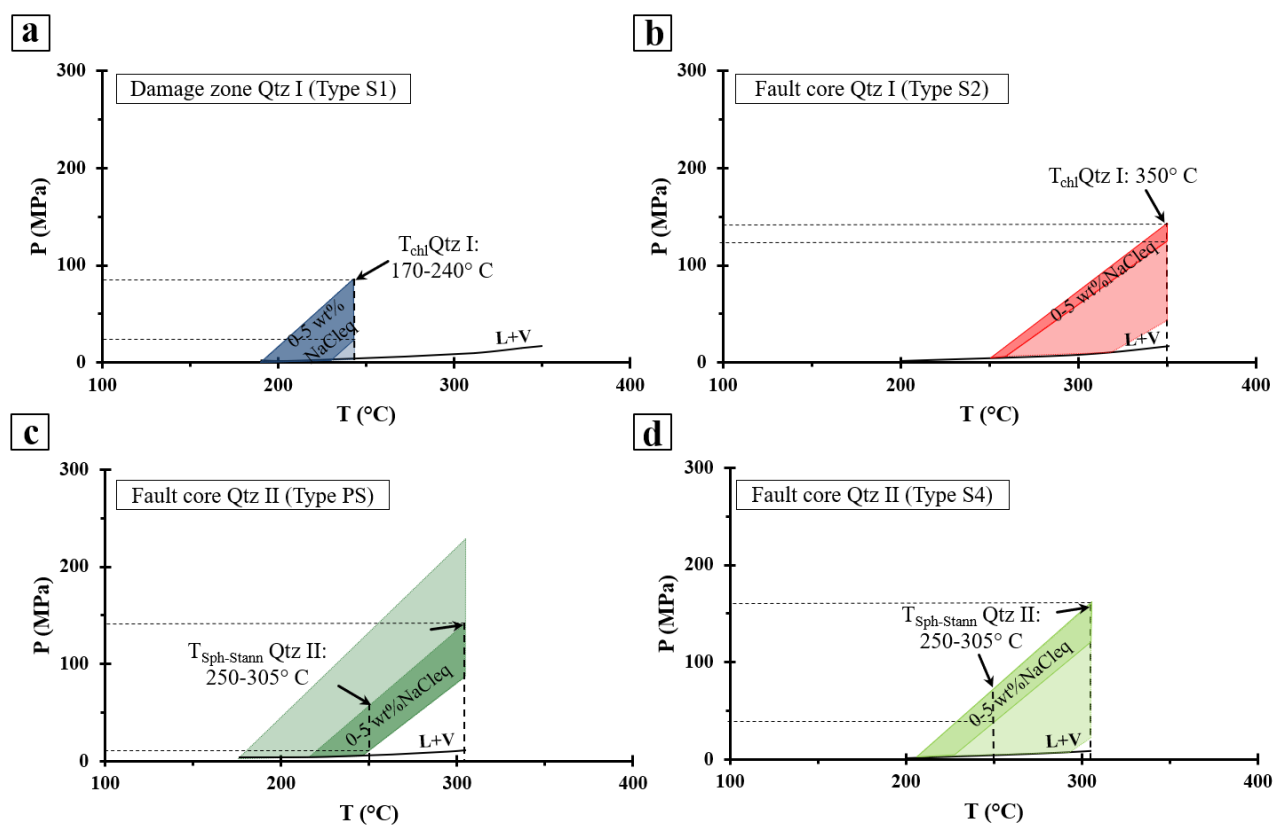
Figure 12. Estimated fluid pressure for the various typologies of FI discriminated petrographically and on the basis of the identified structural domains. Fluid pressures are related to (a) damage zone Qtz I, (b) fault core Qtz I, (c-d) fault core Qtz II. The light-coloured areas are defined by the uppermost and lowermost sets of fluid inclusion isochores, while the dark-coloured areas are related to the pressure range calculated for isochores computed for the most probable composition of the pristine fluid (salinity between 0 and 5 wt%NaCleq, see text for more details). The pressure-temperature areas are also defined by the mineral pairs thermometry (dotted vertical lines), and by the liquid-vapour equilibrium curves for the H_2O-NaCl model fluid. The 240 °C vertical line represents the equilibrium temperature between chlorite and damage zone Qtz I. The 350 °C vertical line is the equilibroum temperature between chlorite and fault core Qtz I. The 250-305 °C vertical lines mark the lowest and highest sphalerite-stannite equilibrium temperature with Qtz II in the BFZ300 fault core. The thick lower curve marks the bundle of liquid-vapour curves for a 1-5 wt% NaCl fault fluid.

977
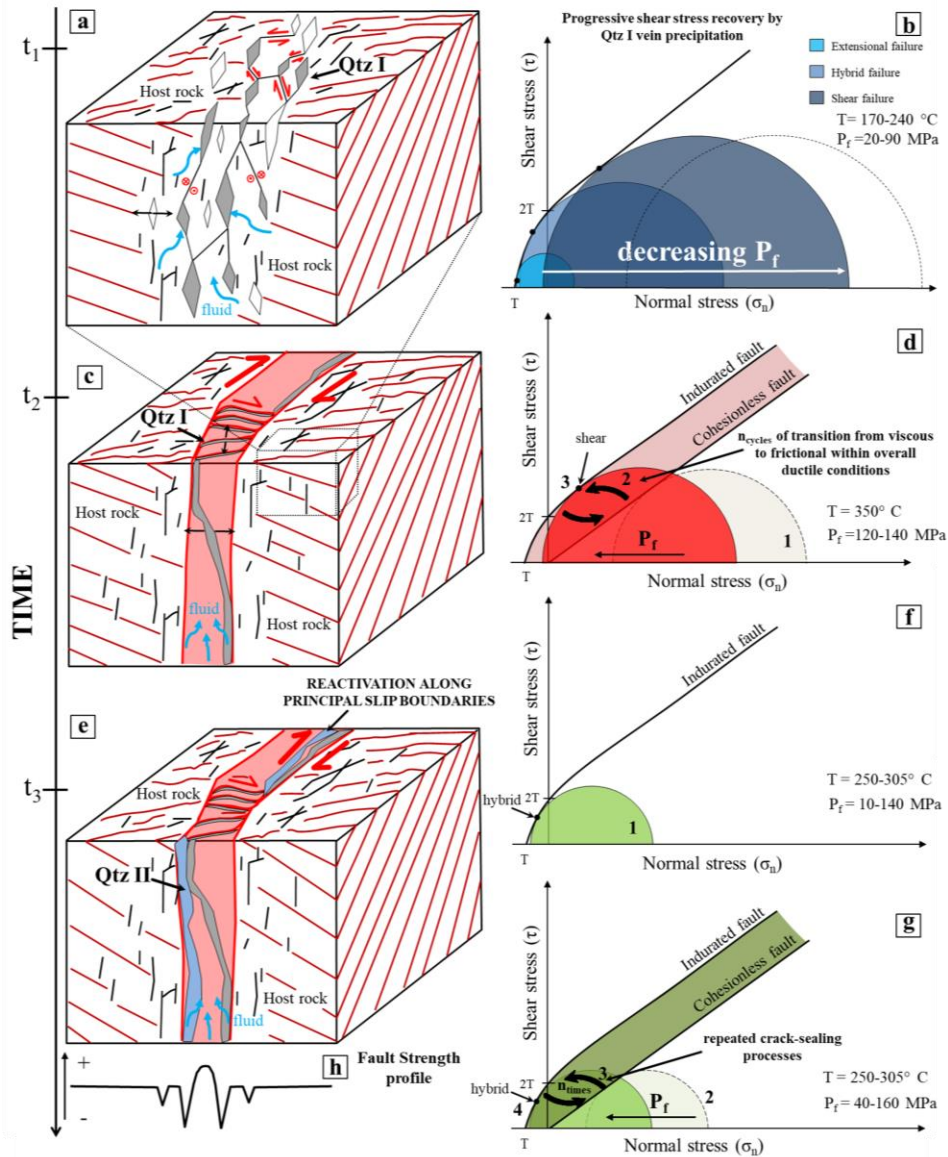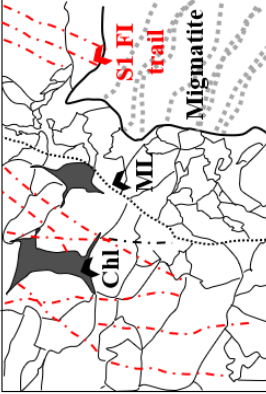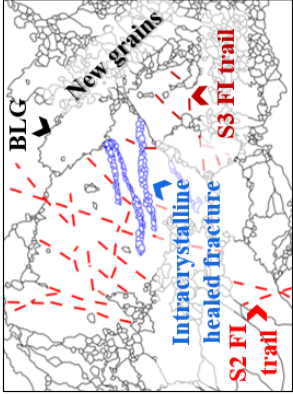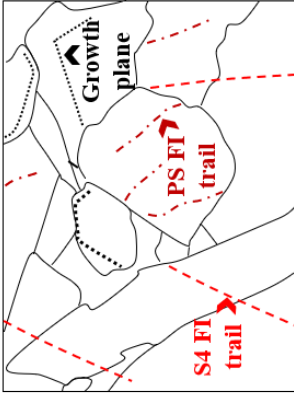
Figure 13. Conceptual model of the temporal and mechanical evolution of the BFZ300 fault zone (see text for more details). Red lines: traces of metamorphic foliation. Black lines: fractures related to the BFZ300 structural development. (a) Initial embrittlement of the migmatitic basement occurred by fracture coalescence under (b) initial lower differential stress conditions and high fluid pressure and followed by a transient increase of differential stress. A first generation of quartz veins (Qtz I) precipitated inside the diffuse network of joints and hydrid/shear fractures which formed during this first deformation stage. (c) Progressive strain localization and fluid channeling within the fault core occurred by (d) episodically renewed fluid-pressure build-up driven by cycles of brittle and ductile deformation. (e-g) Progressive exhumation and cooling of the fault system occurred concomitant with several brittle reactivation episodes of the fault zone under hybrid conditions and fluid pressure lower than during the previous deformational stages. Lastly, a second generation of quartz veins (Qtz II) was emplaced, mainly along the principal slip boundaries of the fault core, following the Qtz I vein as shown by (h) the strenght profile across the fault architecture, that suggests lower tensile strength values (and hence higher reactivation potential) along the Qtz I vein / host rock walls.

988   Table 1: Schematic summary of main microstructures, fluid properties, and PT deformation conditions in the quartz veins of the BFZ300 fault.

Structural zone and sample	Qtz type	Deformation type	Microstructures	Fluid properties: salinity and Thtot	P/T conditions
Damage zone (PH-21)	Qtz I	Brittle/Ductile		Type S1: 0-9 wt%NaCleq Type S1: 150-330 °C	$T_{chl-qtz}$: 170-240 °C P_f (Type S1) 20-90 MPa
Fault core (TPH120-4A)	Qtz I	Cyclic Brittle/Ductile		Type S2: 0-6 wt%NaCleq Type S2: 150-420 °C	$T_{chl-qtz}$: 350 °C P_f (Type S2) 120-140 MPa
Fault core (TPH120-6)	Qtz II	Brittle		Type PS: 0-15 wt%NaCleq Type PS: 160-440 °C Type S4: 0-11 wt%NaCleq Type S4: 150-430 °C	$T_{chl-qtz}$: 160-210 °C $T_{fe-Zn\,part.}$: 220-305 °C P_f(Type PS): 10-140 MPa P_f(Type S4): 40-160 MPa

Note: microstructures are coupled with the corresponding FI types and PT constraints derived from the collected dataset. See text for more explanations. Notice that we combine structural and geochemical data to constrain the relationships between stages of mineral-scale deformation and fluid circulation, which in turn defines the relative chronology of stages of fluid flow during faulting.
ML: median line; Blg: bulging.

1000

Table 2: Chlorite EPMA from various structural zones of BFZ300

Sample	4A	4A	4A	4A	4A	4A	PH21	PH21	PH21	2	2	2	6	6	6	6
Structural zone	FC	FC	FC	FC	FC	FC	DZ	DZ	DZ	DZ	DZ	DZ	FC	FC	FC	FC
Quartz type	Qtz I	Qtz I	Qtz I	Qtz I	Qtz I	Qtz I	Qtz I	Qtz I	Qtz I	Qtz I	Qtz I	Qtz I	Qtz II	Qtz II	Qtz II	Qtz II
Textural type	Verm	Verm	Verm	Rad	Rad	Rad	Verm	Verm	Verm	Verm	Verm	Verm	Rad	Rad	Rad	Rad
Na_2O	0.04	0.07	0.00	0.08	0.08	0.03	0.05	0.02	0.04	0.03	0.01	0.05	0.04	0.06	0.01	0.01
TiO_2	0.02	0.01	0.00	0.00	0.03	0.01	0.09	0.04	0.01	0.01	0.01	0.03	0.03	0.03	0.04	0.13
MnO	0.59	0.65	0.62	0.53	0.56	0.48	0.24	0.24	0.30	0.48	0.37	0.43	0.64	0.57	0.71	0.60
K_2O	0.06	0.02	0.04	0.07	0.06	0.04	0.01	0.01	0.03	0.10	0.05	0.07	0.03	0.02	0.05	0.01
MgO	13.66	13.79	13.74	6.61	5.13	6.75	13.95	14.06	13.29	12.85	12.57	12.59	4.85	4.87	8.73	8.05
SiO_2	25.49	26.00	25.83	23.62	22.89	23.91	27.24	27.02	27.49	27.43	27.88	27.79	25.63	25.64	26.5	26.13
Cr_2O_3	0.00	0.01	0.04	0.00	0.00	0.06	0.04	0.03	0.06	0	0.06	0.01	0	0.02	0.01	0
FeO	27.86	27.74	27.87	36.61	38.49	36.75	24.68	25.21	26.07	25.97	26.06	25.77	34.26	33.84	30.08	30.47
CaO	0.03	0.04	0.05	0.00	0.06	0.03	0.01	0.02	0.02	0.05	0.05	0.03	0.01	0.04	0.04	0.02
Al_2O_3	22.04	22.13	22.00	22.89	23.35	22.98	24.13	24.75	24.91	24.02	23.48	23.21	24.23	24.64	24.49	25.02
Cl	0.00	0.00	0.01	0.03	0.02	0.04	0.01	0	0	0.01	0	0	0.03	0.02	0.02	0.01
Total	89.78	90.45	90.20	90.44	90.67	91.09	90.69	91.42	92.23	91.12	90.81	90.08	89.82	89.94	90.78	90.48
No. ions in formula Based on 28 (O,OH)																
Na	0.02	0.03	0	0.03	0.03	0.01	0.02	0.01	0.01	0.01	0.01	0.02	0.02	0.03	0	0.01
Ti	0	0	0	0	0	0	0.01	0.01	0	0	0.01	0	0.01	0.0	0.01	0.02
Mn	0.10	0.11	0.11	0.10	0.10	0.09	0.04	0.04	0.05	0.08	0.06	0.07	0.12	0.10	0.12	0.11
K	0.01	0	0.01	0.02	0.02	0.01	0	0	0.01	0.02	0.01	0.02	0.01	0	0.01	0
Mg	4.25	4.25	4.25	2.14	1.68	2.17	4.18	4.19	3.93	3.86	3.79	3.82	1.55	1.55	2.69	2.49
Si	5.32	5.37	5.36	5.14	5.02	5.15	5.48	5.40	5.46	5.53	5.64	5.66	5.49	5.47	5.48	5.43
Cr	0	0	0.01	0	0	0.01	0.01	0	0.01	0	0.01	0	0	0	0	0
Fe^{2+}	4.86	4.79	4.83	6.66	7.06	6.62	4.15	4.21	4.33	4.38	4.40	4.39	6.14	6.04	5.20	5.29
Ca	0.01	0.01	0.01	0	0.01	0.01	0	0	0	0.01	0.01	0.01	0	0.01	0.01	0
Al	5.42	5.39	5.38	5.86	6.04	5.84	5.72	5.83	5.83	5.71	5.59	5.57	6.12	6.20	5.97	6.13
Cl	0	0	0	0.01	0.01	0.01	0	0	0	0	0	0	0.01	0.01	0.01	0
Fe	4.86	4.79	4.83	6.66	7.06	6.62	4.15	4.21	4.33	4.38	4.40	4.39	6.14	6.04	5.20	5.29
Al Tetr	2.68	2.63	2.64	2.86	2.98	2.85	2.52	2.60	2.54	2.47	2.37	2.34	2.51	2.53	2.52	2.57
Al Oct	2.73	2.76	2.73	3.00	3.06	2.99	3.20	3.22	3.29	3.24	3.23	3.23	3.61	3.67	3.45	3.56
Based on 28 (O,OH)																
R^{2+}	9.11	9.04	9.08	8.80	8.74	8.79	8.33	8.40	8.26	8.24	8.19	8.21	7.69	7.59	7.90	7.79
Si	5.32	5.37	5.36	5.14	5.02	5.15	5.48	5.40	5.46	5.53	5.64	5.66	5.49	5.47	5.48	5.43
Based on 14 (O,OH)																
R^{2+}	4.55	4.52	4.54	4.40	4.37	4.40	4.17	4.20	4.13	4.12	4.10	4.10	3.84	3.79	3.95	3.89
Si	2.66	2.68	2.68	2.57	2.51	2.58	2.74	2.70	2.73	2.77	2.82	2.83	2.75	2.74	2.74	2.71

1001 Table 3: Representative EPMA of sulphides associated with Qtz II

Analysis	Structural zone	Qtz type	Mineral	S	Fe	Cu	As	Pb	Ni	Zn	Ti	Sn	Total
TPH120-6-14	Core	II	pyrite	55.02	47.50	0.01	0.00	0.00	0.02	0.00	0.00		102.55
TPH120-6-17	Core	II	pyrite	54.08	47.19	0.00	0.01	0.00	0.00	0.00	0.00		101.28
TPH120-6-18	Core	II	sphalerite	34.46	6.46	0.09	0.01	0.00	0.03	59.62	0.02		100.69
TPH120-6-19	Core	II	sphalerite	34.48	6.24	0.08	0.06	0.00	0.04	59.61	0.02		100.53
TPH120-4A-34	Core	II	pyrite	54.49	47.40	0.05	0.00	0.00	0.00	0.00	0.00		101.94
TPH120-4A-35	Core	II	pyrite	54.13	47.26	0.02	0.04	0.00	0.00	0.01	0.55		102.01
TPH120-4A-38	Core	II	galena	13.40	0.00	0.00	0.00	86.63	0.00	0.32	0.01		100.36
TPH120-4A-59	Core	II	galena	13.50	0.06	0.00	0.01	87.04	0.00	0.10	0.01		100.72
TPH120-4A-40	Core*	II	sphalerite	35.06	9.46	0.05	0.00	0.00	0.00	56.74	0.01		101.32
TPH120-4A-43	Core*	II	sphalerite	34.69	9.04	0.01	0.03	0.00	0.00	57.51	0.01		101.28
TPH120-4A-41	Core	II	chalcopyrite	35.40	30.53	33.51	0.00	0.00	0.00	1.32	0.00		100.76
TPH120-4A-42	Core	II	chalcopyrite	35.78	30.78	33.59	0.03	0.00	0.01	1.22	0.01		101.42
TPH120-4A-19	Core **	II	stannite	29.79	12.53	28.41	0.07	0.08	0.00	0.92	0.000	27.86	99.66
TPH120-4A-22	Core **	II	sphalerite	33.82	8.15	0.06	0.00	0.03	0.02	57.27	0.006	0.00	99.36

1002 Note: * - located within cataclastic band and close to stylolite. ** - located along stylolite
1003 Sphalerite and stannite compositions from locations indicated by ** have been used to calculate the temperatures of sphalerite-stannite equilibrium
1004 following the geothermometer of Shimizu and Shikazono (1985). See text for more explanations.